Research Square

Preprints are preliminary reports that have not undergone peer review. They should not be considered conclusive, used to inform clinical practice, or referenced by the media as validated information.

Drug quantification in single 3D organoids reveals correlation to reported in vivo brain uptake and demonstrates translational relevance for prediction of blood-brain barrier permeability

Cindy Bay
Heidelberg University https://orcid.org/0000-0003-3898-3148
Meike Kästing
Heidelberg University
Jiayi Chu
Heidelberg University
Eric Mühlberg
Heidelberg University https://orcid.org/0000-0002-0294-3120
Camilo Scherkl
Heidelberg University https://orcid.org/0009-0008-8569-1694
Philipp Uhl
Heidelberg University https://orcid.org/0000-0002-8616-5599
Julia Carolin Stingl
Heidelberg University https://orcid.org/0000-0002-1566-8156
Jürgen Burhenne
Heidelberg University https://orcid.org/0000-0002-2190-1698
Gzona Bajraktari-Sylejmani
Heidelberg University https://orcid.org/0000-0001-7870-1542
Max Sauter
Heidelberg University https://orcid.org/0000-0003-4977-1925
Johanna Weiss
Johanna.Weiss@med.uni-heidelberg.de
Heidelberg University https://orcid.org/0000-0002-2034-923X

Research Article

Keywords: 3D blood-brain barrier organoids, blood-brain barrier, paracellular marker, permeability, liquid chromatography tandem mass spectrometry, drug screening, New Approach Methodologies

Posted Date: October 21st, 2026

DOI: https://doi.org/10.21203/rs.3.rs-11433171/v1

License: This work is licensed under a Creative Commons Attribution 4.0 International License.
Read Full License

Additional Declarations: The authors declare no competing interests.

Drug quantification in single 3D organoids reveals correlation to reported *in vivo* brain uptake and demonstrates translational relevance for prediction of blood-brain barrier permeability

Cindy Bay[1], Meike Kästing[1], Jiayi Chu[1], Eric Mühlberg[2,3], Camilo Scherkl[1], Philipp Uhl[3,4], Julia Carolin Stingl[1], Jürgen Burhenne[1], Gzona Bajraktari-Sylejmani[1], Max Sauter[1,†], Johanna Weiss[1,†,*]

1) Heidelberg University, Medical Faculty Heidelberg / Heidelberg University Hospital, Internal Medicine IX - Department of Clinical Pharmacology and Pharmacoepidemiology, Im Neuenheimer Feld 410, 69120 Heidelberg, Germany
2) Heidelberg University, Medical Faculty Heidelberg / University Hospital Heidelberg, Department of Nuclear Medicine, Heidelberg University Hospital, Im Neuenheimer Feld 400, 69120 Heidelberg, Germany
3) Heidelberg University, Institute for Pharmacy and Molecular Biotechnology, Department of Pharmaceutical Technology and Biopharmacy, Im Neuenheimer Feld 329, 69120 Heidelberg, Germany
4) Aalen University, Faculty of Chemistry, Beethovenstraße 1, 73430 Aalen, Germany

† These authors contributed equally to this work

[*] Corresponding author:

Prof. Dr. Johanna Weiss

Heidelberg University, Medical Faculty Heidelberg, Heidelberg University Hospital, Internal Medicine IX – Department of Clinical Pharmacology and Pharmacoepidemiology, Im Neuenheimer Feld 410, 69120 Heidelberg, Germany

Tel: +49-6221/5639402

Fax: +49-6221/564642

Email address: johanna.weiss@med.uni-heidelberg.de

Abstract:

Evaluation of blood-brain barrier (BBB) permeability is a crucial step in drug research and development, particularly for the pharmacotherapy of targets in the central nervous system. Current preclinical permeability predictions are hindered by limited transferability or BBB model inaccessibility for analysis. In order to generate relevant pharmacological data, it is necessary to establish qualified physiological, translational, and quantitative systems with validated methods.

3D BBB organoids composed of human cerebral microvascular endothelial cells (hCMEC/D3), and primary pericytes and astrocytes were generated. The BBB barrier function was evaluated using the paracellular marker D-Tyr(Me)Orn. Confocal laser scanning microscopy was used to determine the architecture of the cell arrangements, crucial BBB hallmarks and the apoptosis rate (cleaved caspase 3). An experimental setup was established to evaluate drug uptake into the organoids using ultra-performance liquid chromatography tandem mass spectrometry (UPLC-MS/MS). The concentration- and time-dependent intraorganoidal drug uptake was determined for 13 drugs, and used to calculate the ratio of intra- and extraorganoidal concentrations. These organoid uptake ratios were subsequently correlated with reported *in vivo* brain-to-plasma ratios. Additionally, the performance of four *in silico* BBB permeability prediction tools was assessed with the *in vivo* data.

Optimal analysis time point was identified as day 3 post self-assembly based on organoid architecture, endothelial coverage and apoptosis rate. Modular barrier properties were shown by a reduction of intraorganoidal D-Tyr(Me)Orn after cell connection were compromised, and potential wash out cross-validated by fluorescent Cy5 in the wash solution. Deming regression demonstrated a correlation with pseudo R^2 of 0.64 between the organoid uptake ratios and reported mammalian *in vivo* brain-to-plasma ratios. In contrast, the *in silico* tools evaluated displayed no correlations with these *in vivo* data.

We established and validated a simple and rapid experimental setup for the UPLC-MS/MS drug quantification into single 3D BBB organoids. We demonstrated that the 3D BBB organoids have translational relevance with regard to human and mammalian *in vivo* BBB permeability. This system therefore qualifies as New Approach Methodology (NAM) and can be used for approximate evaluation of *in vivo* brain uptake, while outperforming state of the art *in silico* models.

53 **Keywords:** 3D blood-brain barrier organoids; blood-brain barrier; paracellular marker; permeability;

54 liquid chromatography tandem mass spectrometry; drug screening, New Approach Methodologies.

55 **Graphical abstract:**

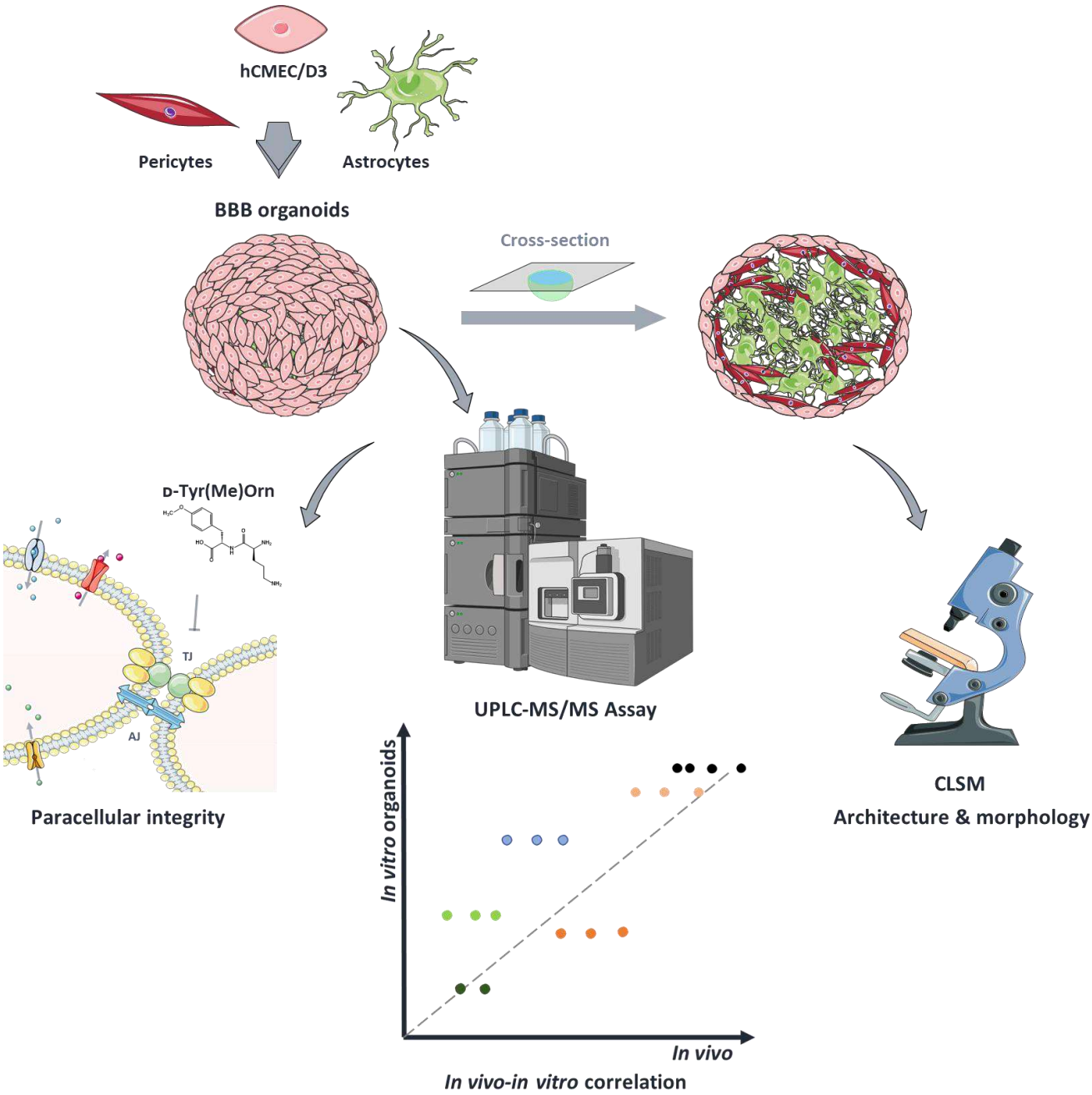

56

Background

The translational relevant evaluation of blood-brain barrier (BBB) permeability in preclinical models is essential for the development of drug candidates, especially for central nervous system (CNS) pathologies. Because the BBB is highly restrictive, the majority of drugs reach minimal exposure in the CNS[1,2]. Currently, many CNS pathologies are still not accessible to efficacious therapeutic options. Although the BBB can be impaired in pathological states such as brain tumors, it can still prevent an effective drug treatment of CNS malignancies. Brain tumors are a type of CNS diseases with a particularly poor prognosis, and they can result in a less restrictive blood-tumor barrier (BTB). But effective pharmacotherapy requires drug access to all cancer cells to prevent relapse. This includes infiltrating cells that are farther away from the BTB and metastases that can often localize behind an intact BBB[3,4].

The scarcity of human BBB permeability data is mainly caused by limited accessibility and invasive sampling as a major hurdle for clinical monitoring of CNS drug exposure. While animal data is abundant, it suffers from the usual limitations of species differences in particular with regard to receptor and transporter mediated uptake and efflux, resulting in remaining uncertainty for clinical efficacy or safety[5-12]. In addition, limiting the use of animals for preclinical research is a main goal for ethically responsible research, with extensive general regulatory support[13-15].

Studies in animals have demonstrated limited predictability of human drug safety and efficacy reflected by the high attrition rate of clinical candidates evaluated with animal toxicological studies[15,16]. In context of BBB permeability, this is especially evident for P-glycoprotein (P-gp) substrates in rodents[5-10]. Many alternative *in vitro* models have historically relied on cell lines and suffer from similar or more pronounced drawbacks of animal experiments in regard to translational relevance[17,18]. The huge variety of current *in vitro* BBB models represents a tradeoff between the physiological replication of the complex BBB architecture and function and accessibility for analysis. Nevertheless, *in vitro* models have decisive advantages. They offer a much higher throughput with lower resource demand and, importantly, help to reduce the number of laboratory animals (e.g. 3R principle: reduce, replace, refine[14]). At the same time, they can be composed entirely of human cells, thus circumventing species differences. Translationally relevant models are therefore urgently required to accelerate drug

85 development. With the rise of New Approach Methodologies (NAMs) and their recent acceptance in
86 toxicological testing by the FDA[15], drug development is undergoing a silent revolution. NAM include
87 human primary cells, induced pluripotent stem cell (iPS)-derived cells, computational models, AI-
88 predictions, organ-on-a-chip, and organoids. Moving to human-centric testing promises more relevant
89 insights into human physiological and biological response, and mechanisms of toxicity. A key
90 prerequisite of NAM use in regulatory preclinical testing is their qualification consisting of the
91 demonstration of their reliability, reproducibility, and the fit-for-purpose. Especially in the context of
92 the BBB, organoid models, like other NAMs, are essential for achieving the interaction between
93 astrocytes, pericytes and endothelial cells that facilitates the most restrictive barrier in human
94 physiology.
95 We aimed to establish a NAM model for BBB permeability and qualify its translational relevance. We
96 selected a simple self-assembling 3D organoid[19,20] that allows direct interaction of endothelial cells,
97 astrocytes, and pericytes as the key BBB architecture. While brain capillary endothelial cells (BCEC),
98 are the main BBB component, the additional cell types have been shown to contribute significantly to
99 BBB establishment and maintenance *in vivo*[21-32] and to the BBB phenotype of endothelial cells *in vitro*[33-
100 47]. These organoids are easy to reproduce and comparatively cost-efficient. They are fully human and
101 the cell types used (hCMEC/D3 and primary astrocytes and primary pericytes) are readily available. In
102 the 3D BBB organoid astrocytes and pericytes can interact freely and are surrounded by a continuous
103 layer of the BCEC hCMEC/D3 cells[20]. Endothelial cells of these organoids express crucial BBB
104 hallmarks, such as Zonula occludens 1 (ZO-1), claudin-5, low density lipoprotein receptor-related
105 protein 1 (LPR-1), the transferrin receptor, and P-gp[20,48]. P-gp-mediated transport was demonstrated to
106 be functionally active[20,49], as was the transcytosis mediated by the transferrin and LRP-1 receptors[20,48].
107 This model has been used for targeting construct assessment, antibody uptake[20,48] and toxicology
108 screening[49]. As an initial proof-of-concept, the penetration of two drugs was qualitatively evaluated with
109 matrix-assisted laser desorption/ionization (MALDI) imaging[19,20]. The presence of a functional barrier
110 was previously mainly demonstrated by increased high molecular marker uptake after tight junction (TJ)
111 opening, like dextran uptake after VEGF treatment[20], which is a limited discriminative marker for the
112 maximal restrictive BBB based on its large size.

113 Our ambition was the development of a translationally qualified permeability methodology based on the
114 optimization of these NAM organoid culture establishing a high-throughput analysis of drug uptake on
115 single organoid level via highly sensitive ultra-performance liquid chromatography tandem mass
116 spectrometry (UPLC-MS/MS) measurements. For this purpose, we investigated the uptake of the
117 validated highly discriminative paracellular marker D-Tyr(Me)Orn[50] and 13 drug (candidates) with
118 known brain concentrations *in vivo* in the context of emerging therapies for brain tumor treatment. Our
119 aim was to establish a NAM for BBB permeability. Therefore, our main objective was to evaluate the
120 *in-vitro-in-vivo* correlation and thereby the translational relevance of the organoid model for the
121 prediction of human BBB permeability.

122 **Methods**

123 **Materials**

124 hCMEC/D3 were purchased from Cellutions Biosystems Inc. (Burlington, Canada), normal
125 hippocampal primary astrocytes from Innoprot (Bizkaia, Spain) and primary human vascular pericytes
126 and Pericyte Medium (PM) from ScienCell Research Laboratories (Carlsbad, CA, USA). Endothelial
127 Growth Medium 2 SingleQuots™ (EGM-2™) and Astrocyte Growth Medium (AGM™) were provided
128 by Lonza (Basle, Switzerland). Roswell Park Memorial Institute (RPMI) 1640 medium was obtained
129 from PAN Biotech (Aidenbach, Germany). Cell+ flasks with vented caps and standard cell culture flasks
130 were purchased from Sarstedt (Nuremberg, Germany).

131 Akura™ 96 spheroid microplates were obtained from Insphero (Schlieren, Switzerland). Antibodies
132 were obtained as followed: mouse anti-human ZO-1 (Invitrogen, Thermo Fisher Scientific, Waltham,
133 MA, USA), mouse anti-human P-gp (BD Biosciences, Heidelberg, Germany), mouse anti-human CD31
134 ab9498 (Dako, Santa Clara, CA, USA), rabbit anti-active caspase 3 (R&D Systems, Minneapolis, MN,
135 USA); goat anti-mouse Alexa-Fluor® 488 secondary antibody (Abcam, Cambridge, UK) goat anti-
136 rabbit Alexa-Fluor® 488 secondary antibody, anti-mouse Alexa-Fluor® 647 secondary antibody
137 (Invitrogen, Thermo Fisher Scientific, Waltham, MA, USA). CellTracker™ Deep Red was also
138 purchased from Invitrogen (Thermo Fisher Scientific, Waltham, MA, USA). Penicillin-streptomycin
139 solution, Dulbecco's phosphate-buffered saline (PBS), Hanks Balanced Salt Solution (HBSS), trypsin-
140 ethylenediamine tetraacetic acid (EDTA) solution (0.5 g porcine trypsin and 0.2 g EDTA/L), fetal
141 bovine serum (FBS), 1 M HEPES buffer, lactate dehydrogenase (LDH) assay, dimethyl sulfoxide
142 (DMSO), Fluoroshield™ with DAPI, adenosine, Triton X-100, human serum (male AB) and
143 collagenase IV were purchased from Sigma-Aldrich (Taufkirchen, Germany). Ethylene glycol
144 tetraacetic acid (EGTA) was purchased from Santa Cruz Biotechnology (Dallas, TX, USA).
145 HumanKine® recombinant human vascular endothelial growth factor (VEGF)165 protein was
146 purchased from Proteintech (Planegg-Martinsried, Germany). Tert-butyl methyl ether (TBME) and the
147 ammonia solution (NH_4OH, aqueous 28%) were provided by Merck (Darmstadt, Germany). CellTiter-
148 Glo® 3D Cell Viability Assay was obtained from Promega (Madison, USA). Human albumin 20% was
149 obtained from CSL Behring (Marburg, Germany). Bovine albumin fraction V (BSA) and Tween®-20

150 were purchased from AppliChem (Darmstadt, Germany). The acetonitrile (ACN), and formic acid (FA)
151 were from Biosolve (Valkenswaard, The Netherlands) all at highest analytical purity. Ultra-purified
152 water was produced with the Arium® mini water system (Sartorius, Göttingen, Germany). Hydrochloric
153 acid (HCl) and sodium hydroxide (NaOH) and were provided by Honeywell (Seelze, Germany).
154 Repotrectinib, futibatinib, lorlatinib, and larotrectinib were purchased from MedKoo Biosciences
155 (Durham, USA); [$^{2}H_{6}$]-futibatinib, [$^{2}H_{3}$,$^{13}C_{1}$]-lorlatinib, [$^{2}H_{4}$]-larotrectinib, temsirolismus and [$^{13}C_{3}$,
156 $^{2}H_{7}$]-temsirolimus were purchased from AlsaChim Shimadzu, (Illkirch-Graffenstaden, France);
157 ulixertinib and [$^{2}H_{6}$]-ulixertinib were obtained from BioMedValley, Asymchem Life Science, (Tianjin,
158 China); olaparib and [$^{2}H_{4}$]-olaparib were purchased from Biozol GmbH (Hamburg, Germany).
159 Selinexor was obtained from Selleckchem (Cologne, Germany), hypericin from Dr. Willmar Schwabe
160 Pharmaceuticals (Karlsruhe, Germany), fluoxetine from Sulpelco Sigma-Aldrich (Taufkirchen,
161 Germany), [$^{2}H_{6}$]-fluoxetine from Cerilliant (Round Rock, TX, USA), octreotide from BACHEM
162 (Bubendorf, Switzerland), [$^{13}C_{6}$]-octreotide from TRC (Vaughan, ON, Canada), paroxetine from EDQM
163 (Strasbourg, France), diazepam from Serva Feinbiochemica (Heidelberg, Germany), senicapoc from
164 MedChemExpress (Monmouth Junction, NJ, USA) and selitrectinib from Hycultec GmbH
165 (Beutelsbach, Germany).
166 The synthesis of D-Tyr(Me)Orn and the stable isotopically labeled D-Tyr([$^{2}H_{3}$]Me)Orn has been reported
167 previously[50].
168 **Stock solutions and dilutions**
169 The drugs were dissolved in PBS with a minimal concentration of DMSO when necessary (generally
170 < 0.1% except for highest concentration of selitrectinib with 1.31% and olaparib with 0.15%). D-
171 Tyr(Me)Orn was stored in a 40 mM stock solution in PBS. All working solutions were freshly prepared
172 after thawing on ice as described in the respective experimental section. The EGTA solution (5 mM)
173 was prepared by diluting the 10 mM EGTA powder in PBS and adjusting the PH to ~ 8 and subsequent
174 dilution in cell culture medium. The 1:10 dilution of trypsin was performed in PBS. Lyophilized VEGF
175 was dissolved in PBS with 1% human serum albumin to a concentration of 100 µg/mL. Adenosine was
176 dissolved in PBS to a concentration of 40 mM. Collagenase IV was dissolved in PBS to a concentration
177 of 15 mg/mL and frozen in aliquots. For organoid lysis, the collagenase IV was thawed and diluted

178 further to 3 mg/mL in PBS. All stock solutions were prepared in their respective solvents and stored in
179 appropriate aliquots at -20 °C.

180 **Cell culture and *in vitro* experiments**

181 hCMEC/D3 cells, primary human astrocytes and pericytes were cultured separately in Cell+ culture
182 flasks in a CO_2 incubator at 37 °C and with 5% CO_2. The hCMEC/D3 cells were kept in EGM-2 medium,
183 the astrocytes in AGM medium and the pericytes in PM medium, each medium mixed with all respective
184 supplements. The cells were washed with HHBSS and detached with trypsin solution for the minimum
185 required time. Detachment was stopped by adding RPMI medium supplemented with a penicillin-
186 streptomycin solution (100 U/mL and 100 µg/mL) and 10% FBS. hCMEC/D3 were used until and
187 including passage 35, astrocytes until passage 5 and pericytes until passage 10 (as previously reported[19]).

188 **Organoid generation**

189 Organoids were generated as described by[19], with the following adaption: 1,500 of each cell type,
190 counted using the MACSQuant® Analyzer (Miltenyi Biotec), were transferred to one well of an Akura™
191 spheroid microplate for self-assembly (day 0). To reduce smaller secondary organoids, the medium was
192 changed after 24 h (day 1). Afterwards, gentle rotation on the rotation shaker in the CO_2 incubator was
193 applied for the remaining culture duration to induce shear stress through flow. Unless otherwise stated,
194 all experiments were performed on day 3 after assembly. As previously published, the organoids were
195 cultured in organoid medium (EGM-2 without VEGF and FBS, supplemented with 2% human serum).
196 This resulted in one organoid per well of the spheroid plate.

197 **Staining and immunofluorescence**

198 For CellTracker™ staining, the described procedure[20] was adapted as follows: cells were stained in the
199 cell culture flask with 5 µM CellTracker™ solution in HHBSS before detachment. After a 15-min
200 incubation at 37 °C, the cells were washed twice with warm HHBSS, detached with trypsin solution and
201 centrifuged. The cells were then gently resuspended in the organoid medium and used for organoid
202 generation. After the respective culture time, the organoids were fixed for 1 h with a 4% formaldehyde
203 solution.

204 For separate or combined immunostaining, the Stemcell™ Technologies protocol „performing
205 immunocytochemical staining of epithelial organoids“ was used for orientation. All incubation steps

206 were performed at room temperature on an orbital shaker and all washing steps lasted 5 min. The
207 organoids were pooled in low-adherence reaction tubes. After formaldehyde fixation, the organoids were
208 incubated for 30 min in a 0.3 M glycine solution and washed three times with an immunofluorescence-
209 buffer (IF-buffer, 0.1% BSA (w/v), 0.2% Triton-X-100 (v/v), 0.05% Tween 20 (v/v) in PBS). The
210 organoids were either directly permeabilized and blocked (5% BSA (w/v), 1% Triton-X-100 (v/v) in
211 PBS) overnight or stored in PBS at 4 °C. After permeabilization staining with the respective primary
212 antibody was performed overnight. The antibodies (CD31, ZO-1, P-gp, Cas3) were diluted 1:100 in IF
213 buffer. After 3 washing steps with the IF buffer, the organoids were incubated overnight with the
214 respective secondary antibody, diluted 1:1000 in buffer (IF-buffer with 10% BSA (w/v)). The organoids
215 were then washed with salt-free water, followed by PBS.
216 To improve imaging quality, all samples were cleared with methanol: after 1 h incubation at room
217 temperature with PBS/methanol (1/1, v/v) a second incubation with 100% methanol was performed.
218 Both steps were carried out at room temperature under gentle agitation. As much methanol as possible
219 was removed and 2 drops of Fluoroshield™ with DAPI were added. Microscopic slides were prepared
220 with thick adhesive tape on both sides. The organoids were slowly transferred to the middle of the slide
221 with a pipette. A cover slip was placed on top of the adhesive film to prevent smashing the organoids.
222 If necessary, more Fluoroshield™ was added to encompass the entire area under the cover slip. The
223 cover slips were left at room temperature overnight to dry for imaging the following day.
224 **Microscopy and image processing**
225 Light sheet microscopy was performed using a Leica DMi1 microscope. Confocal laser scanning
226 microscopy (CLSM) was performed at the Nikon Imaging Center of Heidelberg University using a
227 Nikon AX eclipse Ti2 with a silicon oil immersion objective (Nikon PLAN APO 40 ×/1,25 SIL λS) and
228 the NIS Elements software (Nikon Instruments, Inc.).
229 Image processing was performed using ImageJ2 (as part of Fiji)[51]. Z-stacks were imaged and used for
230 maximum intensity projections and orthogonal views. The organoid circumference was determined
231 using the measurement function for the region of interest (ROI). Brightness and contrast adjustments
232 were always applied linearly over the entire image. These parameters were set qualitatively for each

233 image. If the settings were identical for quantitative comparison, this is indicated under the respective
234 figure.
235 For the quantitative analysis of cleaved caspase 3 (Cas3) staining, the proportion of the positive region
236 in the ROI (the entire organoid area in the respective z-slice) was determined. Therefore, raw
237 unprocessed 16-bit images were used. The respective fluorescence channel was separated and the
238 positive proportion was determined using the threshold function in ImageJ. At equal intervals 3 z-slices
239 within the first 50 µm of each organoid were analyzed. The results for each staining, imaging and
240 organoid generation were normalized to the respective mean of the day 3 sample.

241 **D-Tyr(Me)Orn and drug uptake in organoids**

242 For all uptake experiments, organoids were generated as described and cultured until day 3. For
243 modulation of paracellular tightness, the endothelial cell layer was compromised with multiple
244 orthogonal approaches by pre-incubation with either 20 or 200 ng/mL of VEGF, 1 and 10 µM of
245 adenosine in organoid medium, 5 mM EGTA, 0.5 mM EDTA solution, or a 1:10 dilution of trypsin in
246 PBS. Incubation times are indicated on the respective graph. The control group was incubated with fresh
247 organoid medium. After pre-incubation, the solutions were removed and 300 µM D-Tyr(Me)Orn in
248 organoid medium supplemented with 7% human serum albumin was added. The samples were then
249 incubated for 1 h at 37 °C under gentle agitation in the CO_2 incubator.

250 For drug uptakes, the respective drug was diluted in organoid medium supplemented with 7% human
251 serum albumin to the concentrations indicated in Table 1. The incubation was performed for the time
252 described in the graphs at 37 °C under gentle agitation in the CO_2 incubator. Time-dependent uptake
253 was performed to determine the steady-state concentration.

254 After the respective incubations, the spheroid plates were placed on ice and washed five times with ice-
255 cold PBS supplemented with 2% BSA, followed by one final wash with pure PBS. As much of the
256 remaining liquid in the wells as possible was removed. The presence of organoids was verified under
257 the light microscope. The organoids were lysed enzymatically by adding 20 µL of collagenase IV
258 (3 mg/mL in PBS) to each well and incubating under agitation for 1 h at 37 °C. Then, 20 µL of trypsin
259 solution was added, and the plate was incubated further at 37 °C for 1 h. Lysis was finalized by adding

260 10 µL of a 28% aqueous ammonia solution. Complete and reproducible lysis was verified under a light
261 microscope.

262 For the fluorescent marker substances hypericin (2 µM) and Cy5 (300 µM), incubation was performed
263 accordingly. After incubation, the organoids were washed and fixed for 1 h with 4% formaldehyde. The
264 organoids were fixed on microscopic slide as described for immunofluorescence analysis with
265 Fluoroshield™ with DAPI. Additionally, the fluorescence in the wash solutions was determined using
266 a SpectraMax® with and without pre-incubation with 200 ng/mL VEGF for 4 h (Cy5: 630/670 nm;
267 hypericin: 590/650 nm).

268 **Viability and cytotoxicity assay**

269 Organoids ($n \geq 3$) were incubated with the respective highest drug concentration for the longest used
270 incubation time, thereby also including the evaluation of the highest DMSO concentration used.
271 Subsequently, viability was determined using the CellTiter-Glo® 3D Cell Viability Assay as
272 recommended by the manufacturer. The sample and reaction solution volumes were set to 50 µL. The
273 negative control was treated with 1% Triton-X-100 and the positive control was left untreated.
274 Background controls were performed for the medium and drug solutions. Luminescence was measured
275 using a SpectraMax® plate reader.

276 Cytotoxicity was measured by adding 100 µL of the incubation supernatant to 100 µL of freshly
277 prepared LDH assay reaction solution. Absorption was determined using a SpectraMax® plate reader at
278 490 nm. The positive and negative controls were reversed by definition. Normalized viability and
279 cytotoxicity were then calculated using the formula:

280 $$viability/cytotoxicity\ [\%] = \frac{sample - negativ\ control}{positive\ control - negative\ control} \times 100$$

281 **Sample preparations and analytical method for D-Tyr(Me)Orn UPLC-MS/MS quantification**

282 D-Tyr(Me)Orn was quantified as previously reported[50]. For organoid samples, 25 µL of the internal
283 standard (IS) D-Tyr([$^2H_3$]Me)Orn were added to approximately 50 µL of lysed organoid. After shaking
284 the solution on a plate shaker and pipetting it up and down, 35 µL were transferred to a new 96-well
285 microtiter plate. Calibration and QC solutions were prepared in the organoid matrix: 1,500 cells of each
286 cell type were incubated as described for organoid lysis with 20 µL of collagenase IV, 20 µL of trypsin

287 solution and 10 µL of 28% aqueous ammonia. This solution was manufactured on a larger scale and
288 stored in aliquots at -20 °C. 50 µL of this matrix were mixed with 25 µL of the IS solution and 35 µL
289 were transferred to a new plate. The respective calibration or QC solution was then added. The remaining
290 sample preparation and UPLC-MS/MS were identical to those published previously[50]. In brief, 25 µl of
291 H_2O/ACN (75/25, v/v) + 0.1% FA were added to the study samples to compensate for the volume of the
292 calibration or QC solution. Then, protein precipitation was performed with 100 µL of ACN + 0.1% FA.
293 After shaking, the plate was centrifuged and transferred into the sample manager of the UPLC-MS/MS
294 system. Quantification was performed on a triple quadrupole system TQ-XS (Waters, Milford, MA,
295 USA) in positive ion mode with collision-induced dissociation using argon gas (CID) after z-
296 electrospray ionization (ESI) and multiple reaction monitoring (MRM).

297 **Drug quantification**

298 All UPLC-MS/MS assays in this study were performed on triple quadrupole tandem mass spectrometers
299 with z-ESI, stepwave optimization and CID (Waters Xevo TQ-XS and two separate TQ-S systems: TQ-
300 S1 was coupled with a Waters Binary Solvent Manager Acquity Classic UPLC®, and TQ-S2 was
301 coupled with UPLC I-class® and Waters Binary Solvent Manager FTN®). The systems were coupled
302 with a Waters Acquity Column and Binary Solvent Manager. The respective analytical parameters of
303 the MS and the chromatography for all drugs tested (Table 1), are listed in Supplement Table S1. The
304 analytical parameters for all drugs were determined by the automatic IntelliStart software after direct
305 infusion into the MS system.

306 Organoid matrix was used as a matrix for calibrator and QC samples, as described for D-Tyr(Me)Orn
307 quantification. To 50 µL of the organoid matrix, 25 µL of the respective IS was added. After thorough
308 mixing, 35 µL of the solution were transferred. Next, 25 µL of the respective calibration and QC
309 solutions were added. For the study samples, each lysed organoid was mixed with 25 µL of the IS, and
310 then 35 µL were transferred into a fresh plate. Sample preparation was then performed as summarized
311 in Table 2. All sample preparations were performed in 96-well plates, and the transfer steps were carried
312 out with a multichannel pipette. Centrifugation steps were performed for 10 min at 1000 × *g* after the
313 protein precipitation. The solvent was evaporated for 15 min at 40 °C under nitrogen. The mass
314 spectrometry and chromatography parameters for olaparib, and ulixertinib have already been published

315 previously[52,53], and the sample preparation and calibration range herein were adapted for the organoid
316 matrix. The UPLC-MS/MS octreotide assay was validated for a first-in-human clinical trial[54] and herein
317 adapted.

318 **Calculation of intraorganoidal concentration and organoid uptake ratio**

319 The intraorganoidal concentrations were calculated based on the approximated organoid volume after
320 UPLC-MS/MS quantification of the respective lysis concentrations. For this purpose, the organoids
321 were considered to be spheres with a radius of 100 µm. The concentration in the organoid before lysis
322 was then calculated by multiplying the measured concentration in the lysis volume by the dilution factor.
323 For all measurements, the concentration in empty but otherwise equally treated wells was determined,
324 and the mean of that background subtracted if relevant.

325 The organoid uptake ratio was calculated and then correlated with the reported brain-to-plasma ratios *in*
326 *vivo*. With the approximation, that:

327 $$\frac{intraorganoidal\ concentration}{incubation\ concentration} \approx \frac{brain\ concentration}{plasma\ concentration}$$

328 Therefore, at each time point after steady-state concentration was achieved, the mean intraorganoidal
329 concentration was divided by the respective incubation concentration at that time point. These means
330 were used as the replicates for subsequent correlation as described in the respective section. The reported
331 *in vivo* ratios of either brain-to-plasma or CSF/unbound brain-to-free plasma concentration were used
332 to calculate the mean with respective error. Unbound plasma concentration was determined based on
333 the respective protein binding to calculate the unbound partition coefficient. If all values were reported
334 with their respective standard deviation (SD), error propagation was used to calculate the error of the
335 mean. If error values were not completely reported, the error was approximated as the standard deviation
336 of the mean.

337 ***In silico* BBB permeability prediction**

338 For the herein tested set of drugs, the respective BBB permeability predictions of four readily available
339 *in silico* tools were determined. These were: quantitative predictions of BBBper
340 (https://bbbper.mdu.ac.in/,[55]) and logBB-Pred (https://ssbio.cau.ac.kr/software/logbb_pred/,[56]) as well

as binary predictions by ADMETboost (https://ai-druglab.smu.edu/admet,[57,58]) and SwissADME (https://www.swissadme.ch/,[59,60]).

In vivo-in vitro and *in vivo-in silico* regression analysis

Regression analyses were performed using R version 4.3.1 (R Foundation for Statistical Calculations, Wien, Austria). For all regression analyses the untransformed correlations and the natural logarithm transformations (on one or both axes) were calculated and compared. Residuals, homoscedasticity, normal distribution and linearity were analyzed using the supporting QQ-plots, residuals vs fitted values, scale-location-diagram and Cook's distance or residuals vs index (Deming).

Because both, the organoid uptake ratios and the literature values were subject to uncertainty, a Deming-regression was performed using the Deming-package. The organoid uptake ratio replicates were used to calculate the mean and SD, to ensure equal weighting. For literature ratios x, not all replicate values were available, so the transformed standard error log(Δx) was estimated as follows:

$$\log(\Delta x) \approx \frac{\Delta x}{x}$$

For repotrectinib the CSF of only one volunteer was reported. The missing SD for the human and primate correlation was calculated using linear regression imputation based on the remaining data of the respective regression.

The 95% confidence intervals for both types of uncertainty were calculated using nonparametric bootstrapping (R=1000 replications).

For the regressions involving values without error (*in silico* tool values), weighted least squares regression were performed calculating 95% confidence intervals with build-in functions. The weights were defined as follows:

$$w = \frac{1}{\Delta y^2}$$

And for natural logarithm transformed values:

$$w_{log} = \frac{1}{(\frac{\Delta y}{y})^2} = \frac{y^2}{\Delta y^2}$$

where w (and w_{log}) represents the statistical weight assigned to each data point in the regression, y the predicted (dependent) variable, and Δy the standard deviation of y.

367 The regressions were evaluated using the regression coefficient R^2, which is calculated as the squared
368 Pearson correlation coefficient. Because Deming regression does not have an associated R^2-type
369 measure, the Pearson correlation coefficient was used as a proxy for linear association strength reported
370 as pseudo-R^2.

371 **Data analysis, statistical methods and illustrations**

372 The Waters TargetLynx V4.2 software (Waters, Milford, MA, USA) was used for quantification with
373 UPLC-MS/MS. This was based on $1/x^2$-weighted linear regressions of the analyte response versus the
374 respective IS response. The resulting calibration curve was used to quantify the study samples. GraphPad
375 Prism was used for standard data visualization and statistical analysis, as indicated on the respective
376 figures. Significances were displayed as follows: $p \leq 0.0001$ ****; $p \leq 0.001$ ***, $p \leq 0.01$ **, $p \leq 0.05$
377 *, p-values over 0.05 were considered not significant. ChemDraw (version 23.1.2) was used to draw the
378 chemical structures and calculated clogP. Microsoft Excel and PowerPoint (Mountain View, CA, USA)
379 were used for data processing and visualization respectively. Figures were created with adapted
380 illustrations from Smart Servier (https://smart.servier.com/), licensed under CC BY 4.0
381 (https://creativecommons.org/licenses/by/4.0/) and illustrations created in BioRender (Bay, C. (2026)
382 https://BioRender.com/yaevw7j), including the graphical abstract.

383

384 ## Results

385 ### Evaluation of 3D BBB organoid architecture

386 The morphology of the cells and their overall organoid architecture were evaluated in detail over the
387 course of the culture time. Therefore, the immunofluorescence and staining protocols were optimized to
388 include the organoid core, with longer incubation times and methanol clearing. Although simultaneous
389 staining with different CellTracker™ dyes would have been preferable, CellTracker™ Deep Red
390 exhibited superior properties compared to the other tested CellTracker dyes (Green CMFDA, Violet
391 BMQC, VivoTrack 680 near infrared), particularly in terms of even distribution throughout the cells
392 over time. Therefore, only this dye in combination with effective CD31 staining of BCEC was used.
393 The architecture of the organoids was imaged in depth over the course of the culture: Fig. 1 shows the
394 organoids from days 2 to 5, with emphasis on the hCMEC/D3 coverage. Detailed images of the astrocyte
395 and pericytes on day 3 are shown in Fig. 2A-D, remaining time points can be found in detail in
396 Supplementary Fig. 1. The morphology of the astrocytes and pericytes was harder to depict after day 4,
397 based on the uneven CellTracker™ staining. The majority of organoids demonstrated correct
398 architecture, while some organoid preparations showed astrocytes on the outside. However, an
399 endothelial layer was present beneath these outside astrocytes (see Supplementary Fig. 2). Additionally,
400 the expression of the crucial BBB hallmarks (ZO-1 and P-gp) and the collagen IV matrix were verified
401 (Fig. 2E).

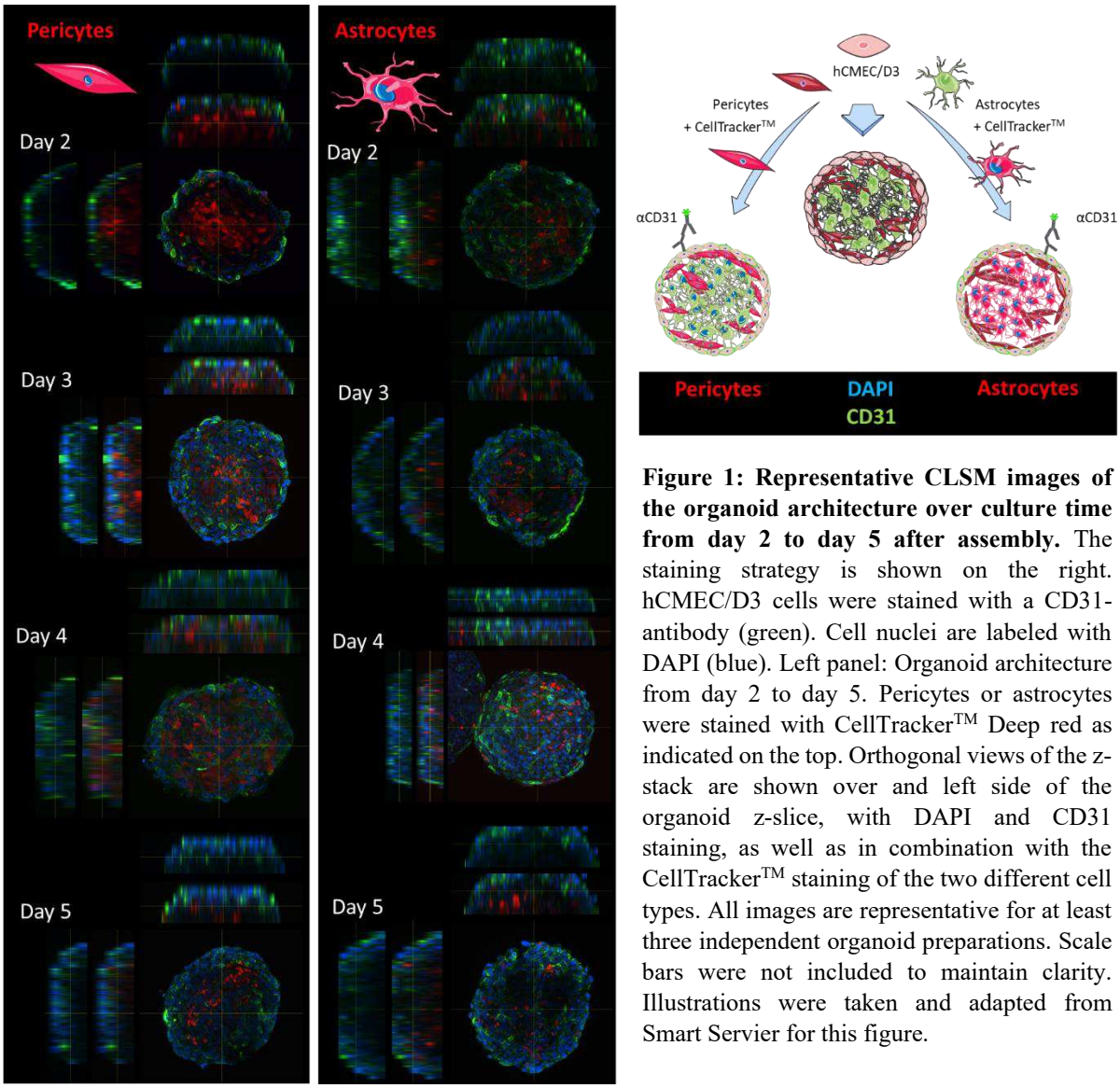

Figure 1: Representative CLSM images of the organoid architecture over culture time from day 2 to day 5 after assembly. The staining strategy is shown on the right. hCMEC/D3 cells were stained with a CD31-antibody (green). Cell nuclei are labeled with DAPI (blue). Left panel: Organoid architecture from day 2 to day 5. Pericytes or astrocytes were stained with CellTracker™ Deep red as indicated on the top. Orthogonal views of the z-stack are shown over and left side of the organoid z-slice, with DAPI and CD31 staining, as well as in combination with the CellTracker™ staining of the two different cell types. All images are representative for at least three independent organoid preparations. Scale bars were not included to maintain clarity. Illustrations were taken and adapted from Smart Servier for this figure.

402

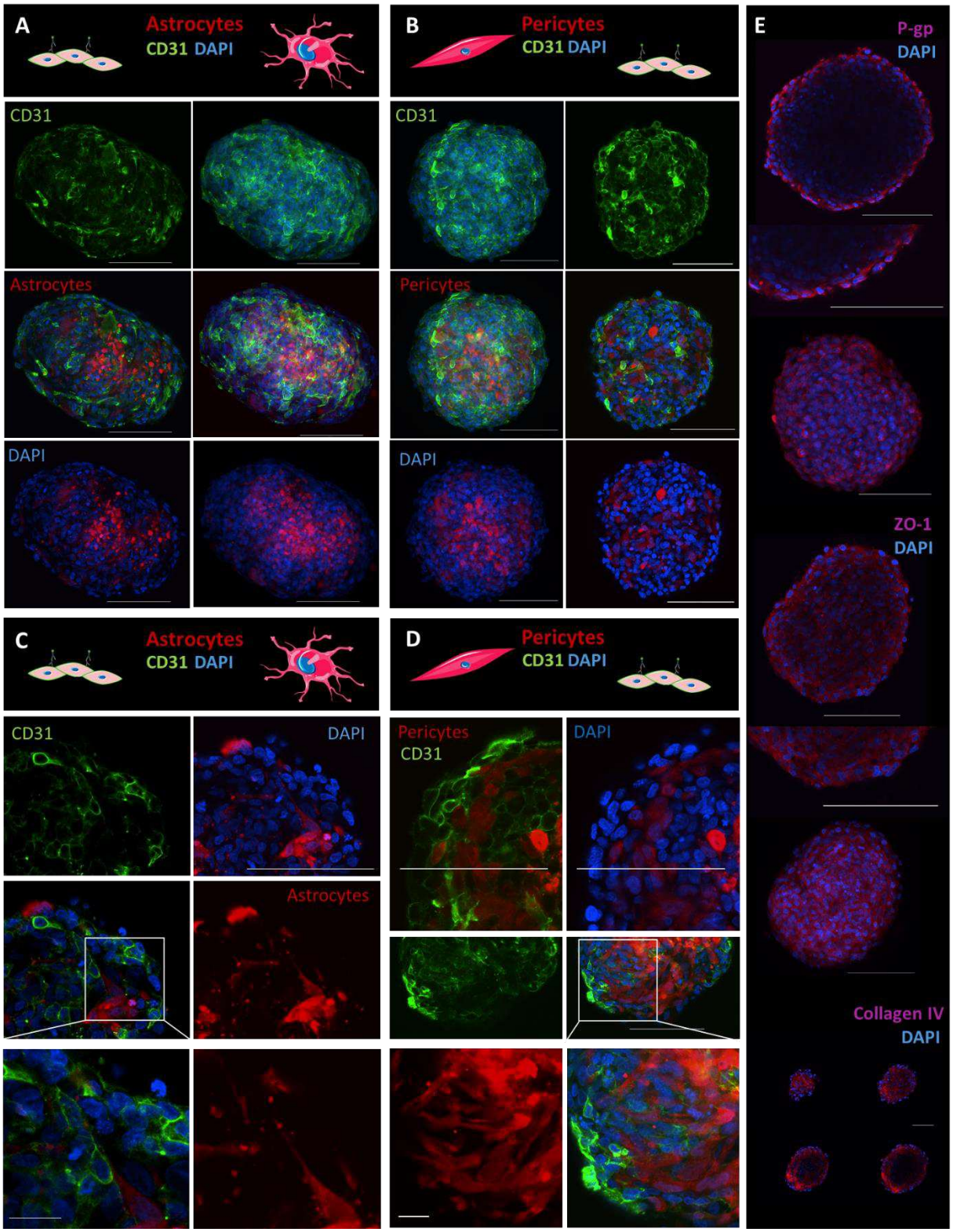

Figure 2: Representative CLSM images of the detailed organoid architecture and cell morphology on day 3. All nuclei were stained with DAPI (blue). Either astrocytes or pericytes were stained with CellTracker™ (red). hCMEC/D3 cells were labeled with anti-CD31 immunofluorescent staining (green) and BBB hallmarks P-gp, ZO-1 and Collagen IV immunolabeled in magenta. **A** Organoids with stained astrocytes (red) and hCMEC/D3 (green), on the left side z-slices with the respective channels are shown and on the right side the corresponding z-projections. **B** Organoids with stained pericytes (red) and hCMEC/D3 (green), on the right side z-slices with the respective channels are shown and on the left side the corresponding z-projections. **C** Detailed view of the astrocytes in the organoid with splitted fluorescence channels. Lowest panels show magnification of the write rectangle, to highlight astrocyte process with end in contact with BCEC. **D** Detailed view of the pericytes in the organoid with splitted fluorescence channels. Lowest panels show magnification of the write rectangle, to highlight

414 cell elongations. **E** Representative immunofluorescence images of organoids (from top to bottom): P-gp
415 immunostaining z-slice, magnification of outer organoid edge and a z-projection; ZO-1 immunostaining z-slice,
416 magnification of outer organoid edge and z-projection; collagen IV immunostaining four ascending z-slices. All
417 scale bars = 100 µm, except in magnifications of **C** and **D** scale bar = 20 µm. All images are representative for at
418 least three independent organoid preparations with each at least three organoid images per experiment. Cell
419 illustrations taken and adapted from Smart Servier.

420 **Evaluation of apoptosis during culture by Cas3 staining**

421 Firstly, the average size (measured as circumference) was determined over time. As depicted in Fig. 3A,
422 the organoids did not grow significantly during the first 5 days, compared to day 2 after assembly. Only
423 on day 6, the circumference was significantly larger. The extent of apoptosis was visualized within the
424 relevant time frame with preferred architecture from day 2 to day 4 using Cas3 immunofluorescent
425 staining. As shown quantitatively in Fig. 3B and with representative images in Fig. 3C, the apoptosis
426 decreases after an initial peak on the day after generation. Over time, the Cas3-positive regions appear
427 to move closer to the surface region of the organoid. Based on these results in combination with the
428 architecture over time, day 3 was selected as the optimal time point for experiments.

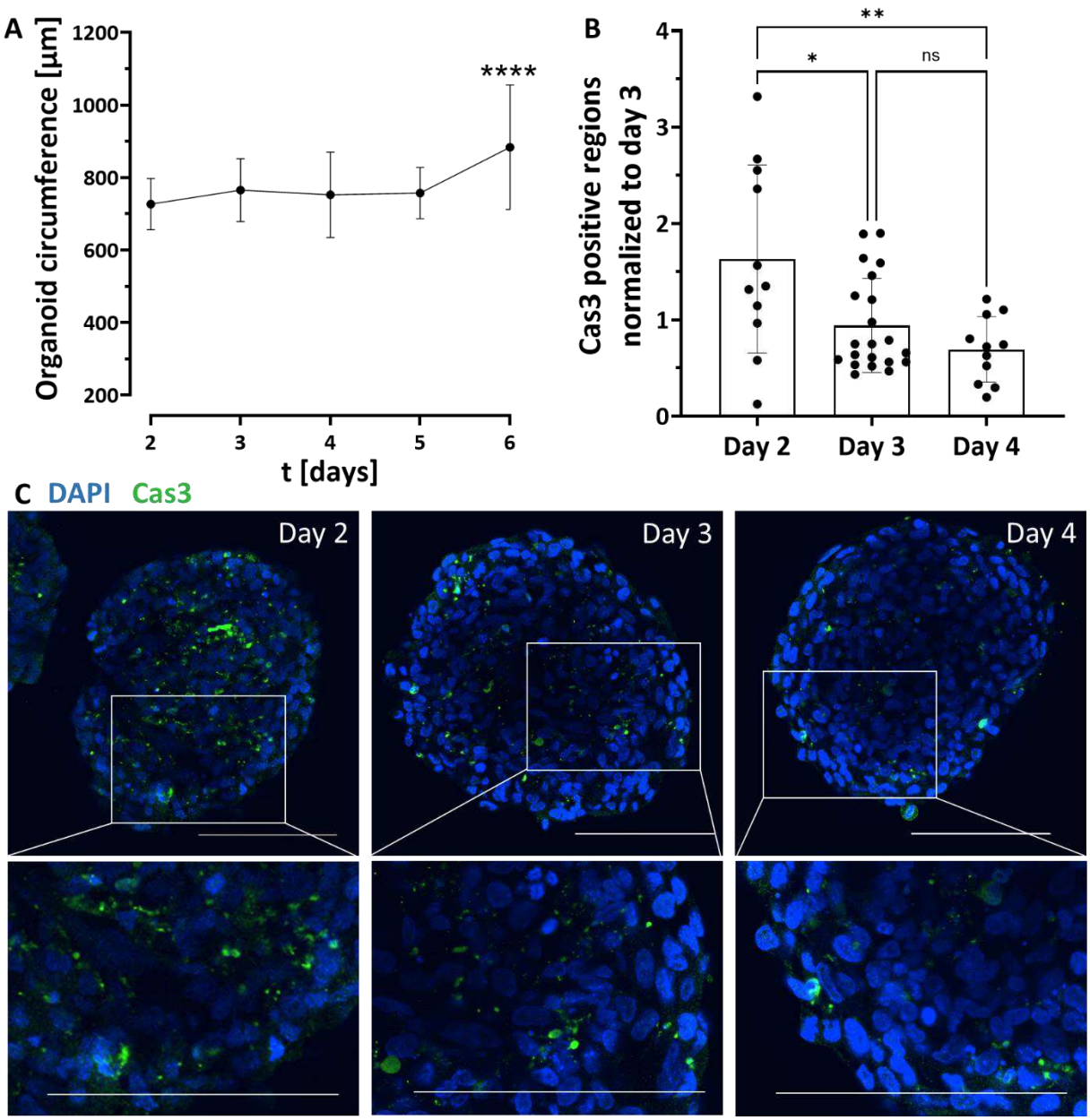

Figure 3: Evaluation of organoid size and apoptosis over time. A Organoid circumference from day 2 to day 6, shown as mean ± SD of at least 18 individual organoids from four independent experiments. Significant enlargement at day 6, one-way ANOVA with Dunnett's posthoc test compared to day 2. **B** Share of Cas3 positive region between day 2 and day 4. Depicted as mean ± SD of at least eleven individual organoids from at least three independent experiments, normalized to day 3 of each experiment. Each point represents one organoid. Statistical analysis with one-way ANOVA with Turkey's correction for multiple testing comparing all groups with each other was performed. **C** Representative CLSM images of Cas3 immunofluorescent staining. On each day an organoid is shown with z-slice and one enlargement as indicated with the white rectangle. Images were processed equal for comparison.

440 **D-Tyr(Me)Orn demonstrates modular paracellular tightness of organoids**

441 Our previously published analytical assay with the established paracellular marker D-Tyr(Me)Orn[50] was
442 validated in the organoid matrix, enabling its use in analyzing the integrity of organoids (Supplement
443 Table S2).

444 To modify the paracellular integrity of the organoids, the cell-to-cell connections were compromised
445 using different modulators: VEGF, adenosine, trypsin, EGTA and EDTA. This pretreatment
446 significantly reduced the amount of the paracellular marker inside the organoids (Fig. 4A-D) indicating
447 an increased washout of D-Tyr(Me)Orn with reduced tightness of the organoids in our experimental
448 setting that requires six washing steps for the required sensitivity of drug uptake quantification. These
449 results are counterintuitive, so we investigated the washout of two small fluorescent compounds using
450 the same settings as before, but with a detection method that has a higher dynamic range: (1) Cy5, a
451 highly hydrophilic marker, which can only reach the inner part of the organoid paracellularly and (2)
452 hypericin, a highly lipophilic compound which can penetrate the endothelial cells via the plasma
453 membrane. The respective distribution of the two marker compounds was evaluated with CLSM (Fig.
454 4G). This revealed a cell staining with the lipophilic fluorescent hypericin, while Cy5 was mainly found
455 in the presumed extracellular space and next to nuclei showing signs of apoptosis verifying the different
456 routes of uptake into the organoids. Quantifying the fluorescence after different washing steps revealed
457 a higher fluorescence of Cy5 in the wash solutions in the VEGF-pretreated group. However, this
458 difference was only significant in the third washing step (Fig. 4E). In contrast, the washout of the
459 lipophilic compound hypericin did not increase in the VEGF-pretreated group, but was even lower in
460 the first washing step after VEGF incubation (Fig. 4F).

461

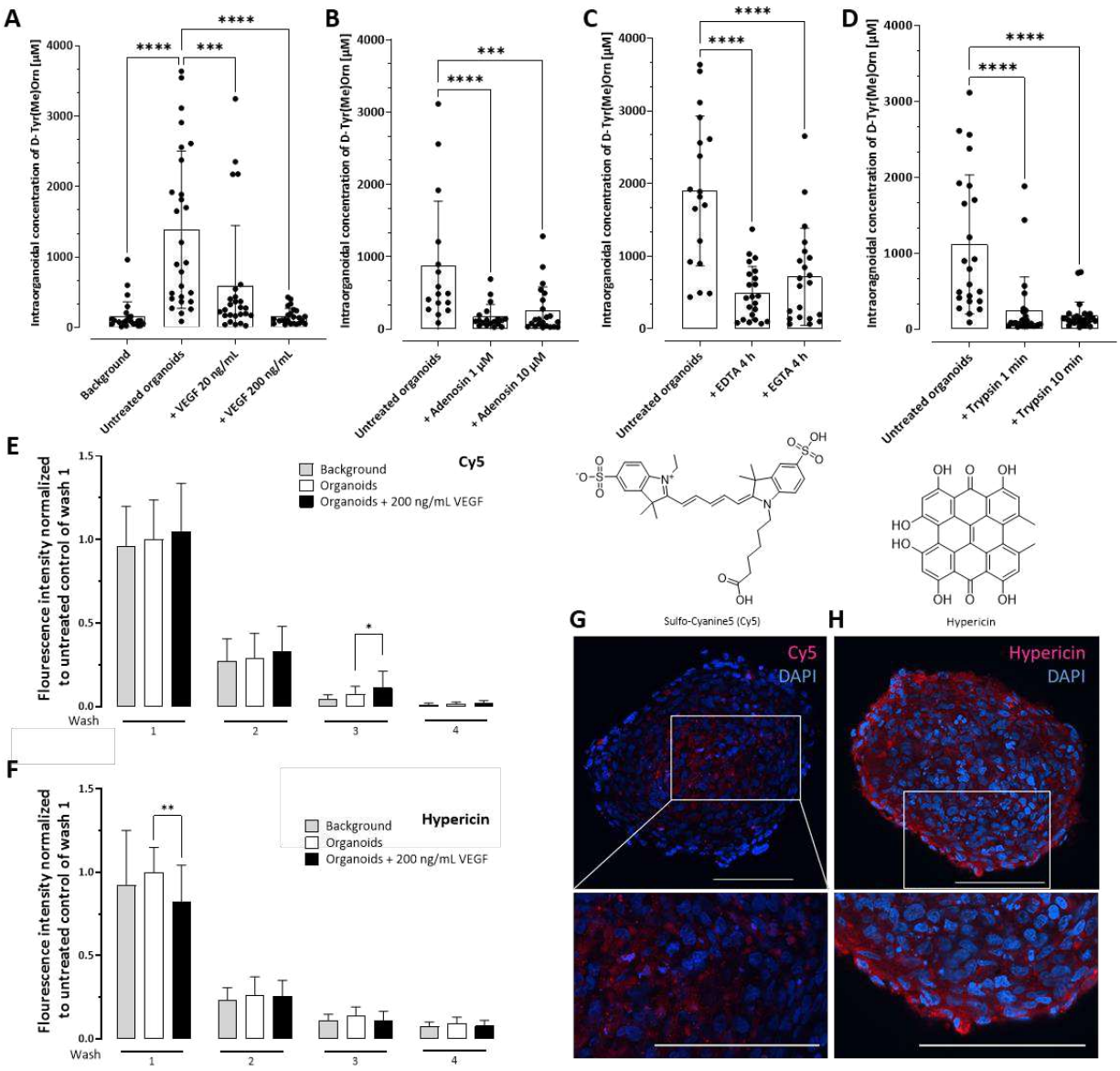

Figure 4: Evaluation of paracellular integrity of the organoids. Cell connections were compromised with the indicated pretreatment **A** 20 or 200 ng/mL VEGF for 4 h, **B** 1 and 10 µM adenosine for 1 h, **C** 5 mM EGTA or 0.5 EDTA solution for 4 h **D** trypsin solution diluted 1:10 for 1 and 10 min after the six washing steps as developed for the UPLC-MS/MS setup. All pretreatments significantly reduced the intraorganoidal concentration of D-Tyr(Me)Orn compared to untreated organoids. Data presented as mean ± SD. Probable outliers were removed with GraphPad Prism. Each point represents an individual organoid from three independent experiments with each at least four organoids. **E** Accordingly, the fluorescence of Cy5 in the wash solution for washing step 3 was significantly higher in the VEGF pretreated group, **F** while the amount was reduced for the lipophilic marker hypericin in washing step 1. **G** Cy 5 and **H** hypericin were also visualized under the fluorescent microscope. Respective structures are depicted on top. These two markers showed a distinct distribution in the organoids (both red): hypericin stained the cells and Cy5 was contained to the extracellular space. Representative z-slices of organoids of three independent experiments, and respective detailed presentation. Cell nuclei stained with DAPI (blue). Scale bar = 100 µm. All statistical analysis were performed with one-way ANOVA with Dunnett's post-hoc test.

478 **Experimental setup for UPLC-MS/MS quantification of drug uptake in organoids**

479 Quantification on single organoid level using UPLC-MS/MS was challenging due to the difficulty of
480 measuring low concentrations in a small number of cells. Transfer steps should be avoided due to the
481 potential for disruption of the barrier. This required an experimental setup with easy access for washing,
482 feasible for automation. Based on the use of spheroid plates, the organoid generation and whole drug
483 exposure until lysis could be performed in one format (Fig. 5). Excessive washing is required due to the
484 tiny intraorganoid volume available for drug uptake in combination with expected low permeation
485 through the hCMEC/D3 layer and the high concentration of substance in the incubation solutions.
486 Additionally, to avoid losing organoids when the solution is removed after incubation and during each
487 washing step, a residual volume of 10 µL must be left in the wells. Six washing steps ensured the
488 required reduction of the background caused by remaining volume of substance solution in the wells (~
489 10 µL remaining, wash with 150 µL) resulting in the possibility to detect intra-organoid concentrations
490 of 1% of the incubation solution. This protocol resulted in an acceptable loss of ~ 5% of the organoids
491 per plate (39 plates with a total of 2,682 organoids, 154 organoids were lost; with a mean loss of
492 5.5 ± 4.0% per plate).

493 A particular challenge for analysis was the organoids resistance to lysis due to the strong cellular and
494 extracellular connections. The organoids were resistant to basic and acidic lysis, organic solvents,
495 vigorous mixing, and ultrasound, in accordance with collagen expression (Fig. 2E). The goal was to
496 completely disassemble the organoids and completely lyse cells for a reproducible lysis protocol and
497 accurate quantification. The final protocol involved enzymatic digestion (1 h collagenase IV and 1 h
498 trypsin/EDTA solution) followed by ammonia lysis. This achieved complete dissolution of the
499 organoids (Supplementary Fig. S3).

500

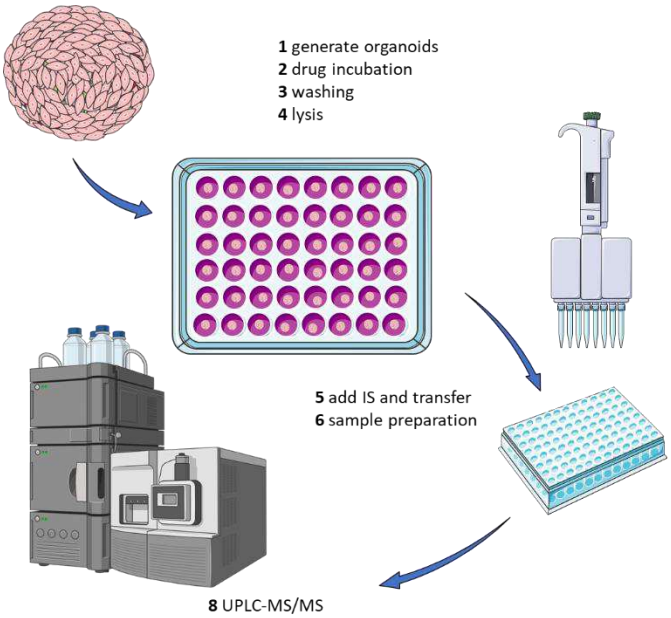

Figure 5: Experimental setup for UPLC-MS/MS assay in 3D BBB organoids. Schematic overview of the organoid assay for UPLC-MS/MS quantification. Organoids are generated directly in the coated spheroid plates and incubated with the respective drug on day 3. After incubation, organoids are washed 6 times and digested with collagenase IV and trypsin. After ammonia lysis, the IS is added. Then, the samples are transferred to a new plate and subjected to the respective sample preparation and UPLC-MS/MS quantification. Created with adapted illustrations from Biorender and Smart Servier.

Correlation of organoid drug uptake with *in vivo* BBB permeability data for evaluation of the translational relevance of the 3D BBB organoid model

All drug quantifications were based on verified calibration curves using QC samples in the organoid matrix (see Supplementary Table 3 for representative QC results). Additionally, the stability of the drugs during the organoid lysis was confirmed. The concentration of the drugs in the organoid was then determined concentration- and time-depended, as depicted in Fig. 6, A. A time-dependent assessment is necessary to identify the relevant concentration equilibrium for accurate organoid uptake ratio calculation. Concentration-dependent assessment is required to identify nonlinear effects, such as transport saturation. All uptakes were performed in three independent experiments. Not all incubations and time points resulted in measurable organoid concentrations. Values were accepted for downstream analysis if at least seven individual organoids from two independent organoid preparations were quantifiable. For octreotide, the concentrations in the organoids equaled the background concentrations and were therefore interpreted as negligible organoid uptake. This zero-point was not used for correlation and only included in the following plots for visualization. Overall, organoid concentration was linear to increasing incubation concentration. Saturation of uptake was achieved for all drugs within the observed time frame. Steady state was presumed, when there was no significant concentration increase between the time points (see Supplementary Table S4). After reaching steady state, the ratio of the mean organoid uptake concentration to the respective incubation concentration was calculated for

520 each time point (= organoid uptake ratio). These ratios, each based on at least ten individual organoids,
521 were used as replicates for the correlation with reported *in vivo* brain-to-plasma ratios (Fig. 6B). The *in*
522 *vivo* data can be seen in detail in Table 3. Either the brain tissue-to-total plasma ratio or the unbound
523 brain- or CSF- to-unbound plasma ratio was used (please refer to the discussion for a detailed description
524 of the literature data). Concentrations too close to the measured background were excluded to avoid
525 artifacts. Reduction of viability and cytotoxic effects were evaluated for all drugs used (Fig. 6C). The
526 quality of the correlation was determined using Deming regression (Fig. 6D-F). A comparison of the
527 mammalian correlations performed with and without transformation can be seen in Supplementary Fig.
528 S4. Based on normality diagnostic plots, a transformation using the natural logarithm of both axes was
529 selected for the final correlation (see Supplementary Fig. S5). This resulted in a pseudo R^2 of 0.64 for
530 the Deming regression between organoid uptake ratios and the complete mammalian data set for *in vivo*
531 brain-to-plasma ratios (Fig. 6, D). Sub-analysis with the reported primate data provided a pseudo R^2 of
532 0.81 (Figure 6, E), and regression solely based on human data resulted in a pseudo R^2 of 0.82 (Figure 6,
533 F).

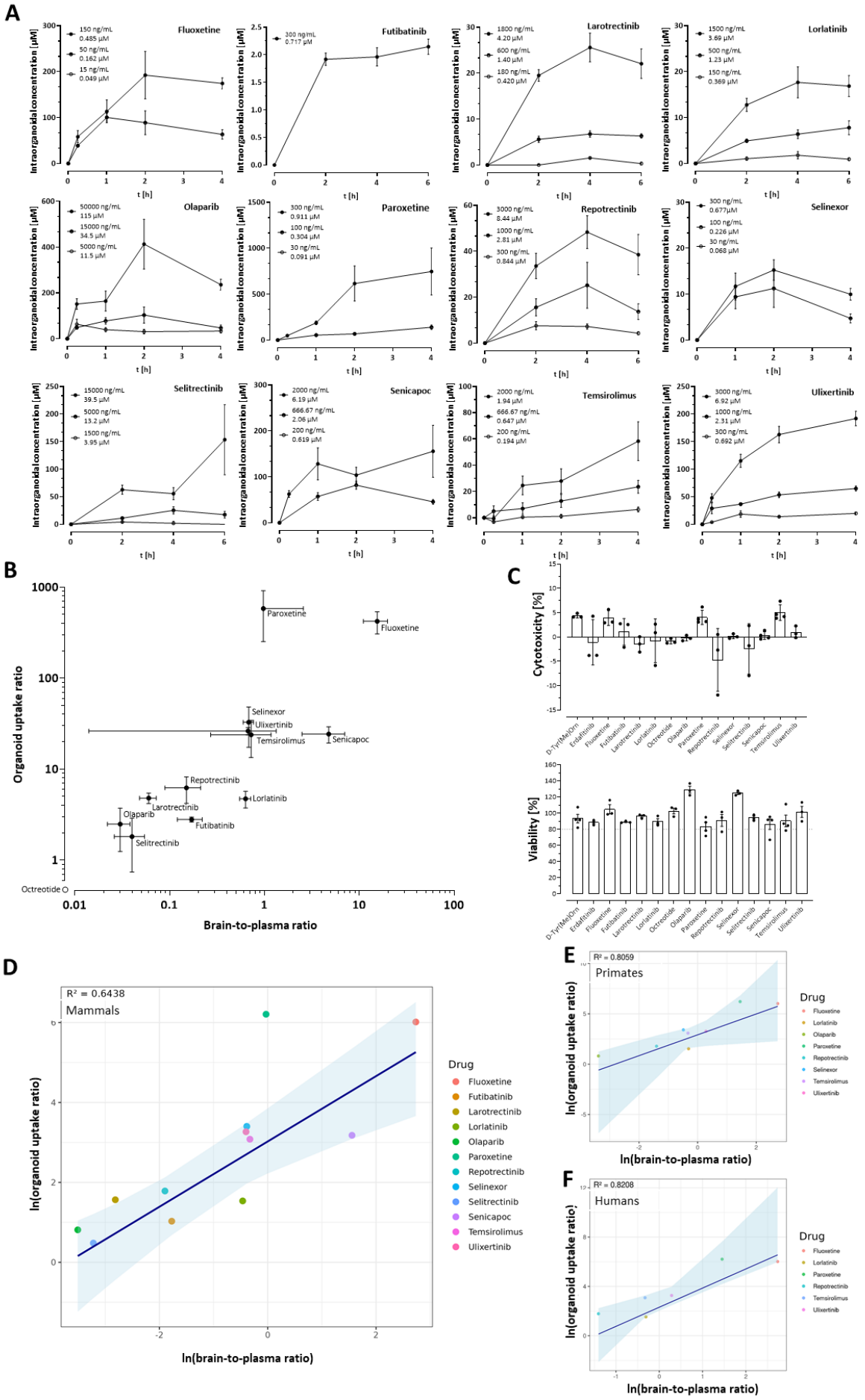
A
Fluoxetine
Futibatinib
Larotrectinib
Lorlatinib
Olaparib
Paroxetine
Repotrectinib
Selinexor
Selitrectinib
Senicapoc
Temsirolimus
Ulixertinib
Intraorganoidalconcentration [µM]
t [h]
B
Organoid uptake ratio
Brain-to-plasma ratio
Paroxetine
Fluoxetine
Selinexor
Ulixertinib
Temsirolimus
Senicapoc
Repotrectinib
Lorlatinib
Larotrectinib
Olaparib
Futibatinib
Selitrectinib
Octreotide
C
Cytotoxicity [%]
Viability [%]
D
R² = 0.6438
Mammals
ln(organoid uptake ratio)
ln(brain-to-plasma ratio)
Drug
Fluoxetine
Futibatinib
Larotrectinib
Lorlatinib
Olaparib
Paroxetine
Repotrectinib
Selinexor
Selitrectinib
Senicapoc
Temsirolimus
Ulixertinib
E
R² = 0.8059
Primates
F
R² = 0.8208
Humans

534

535 **Figure 6: A** Concentration-time profile of the quantified drugs in the organoid. These were used to determine the
536 steady state time and to calculate the respective organoid uptake ratios for the correlation. Data depicted as mean
537 ± SEM of at least seven organoids from at least two independent organoid preparations**. B** Correlation of organoid
538 uptake ratios with reported *in vivo* brain-to-plasma ratios. The quantified drug concentrations in the organoid were
539 used to calculate the ratio to the incubation concentration (organoid uptake ratio). These are depicted against the
540 reported *in vivo* brain-to-plasma ratios (Table 3). Data is shown as mean ± error calculated as described in the
541 method section. Based on logarithmic axis, the zero data point of octreotide cannot be depicted and was inserted
542 afterwards for conceptual visualization. **C** Viability (ATP) and Cytotoxicity (LDH) after incubation with the
543 highest used concentration for the longest observed time point. Mean ± SD of at least three replicates. Each point
544 represents an individual organoid. **D** Deming regression of the measured organoid uptake ratios with reported
545 mammalian *in vivo* brain-to-plasma ratios and **E** with only the reported primate *in vivo* data and **F** only the human
546 *in vivo* data. The correlations were performed using natural logarithm-transformed data. Respective pseudo R^2 and
547 the 95% confidence interval are depicted. The Deming regression calculated the insecurities of both axes. Data
548 points represent the mean of the ratios of the individual drugs, the error values were transformed as described in
549 the method section.

550

551 **Regression of the *in vivo* BBB permeability data set with results from *in silico* BBB prediction**
552 **tools reveals absent linear correlation**

553 For the selected drug set, the BBB permeability predictions of four *in silico* web tools were determined
554 and correlated with the researched *in vivo* data set. Two of the tools provided quantitative results: the
555 BBB Score [%] of ADMETboost and logBB-values of the logBB-Pred tool (Fig. 7A and B). As
556 performed for the correlation with the organoid uptake data, natural logarithm transformations were
557 performed, and the best hits were presented (Fig. 7C and D, comparisons of direct and transformed
558 correlations are in Supplementary Fig. 4, transformed diagnostic plots are in Supplementary Fig. S5).
559 Because only the *in vivo* data had a reported error, a weighted regression was performed. However, no
560 linear correlation was seen for the selected drug set with either tool (R^2 of 0.06 and 0.13). The binary
561 results (BBB permeable/non-permeable) of SwissADME and BBBper also did not result in a meaningful
562 pattern (Fig. 7E and F).

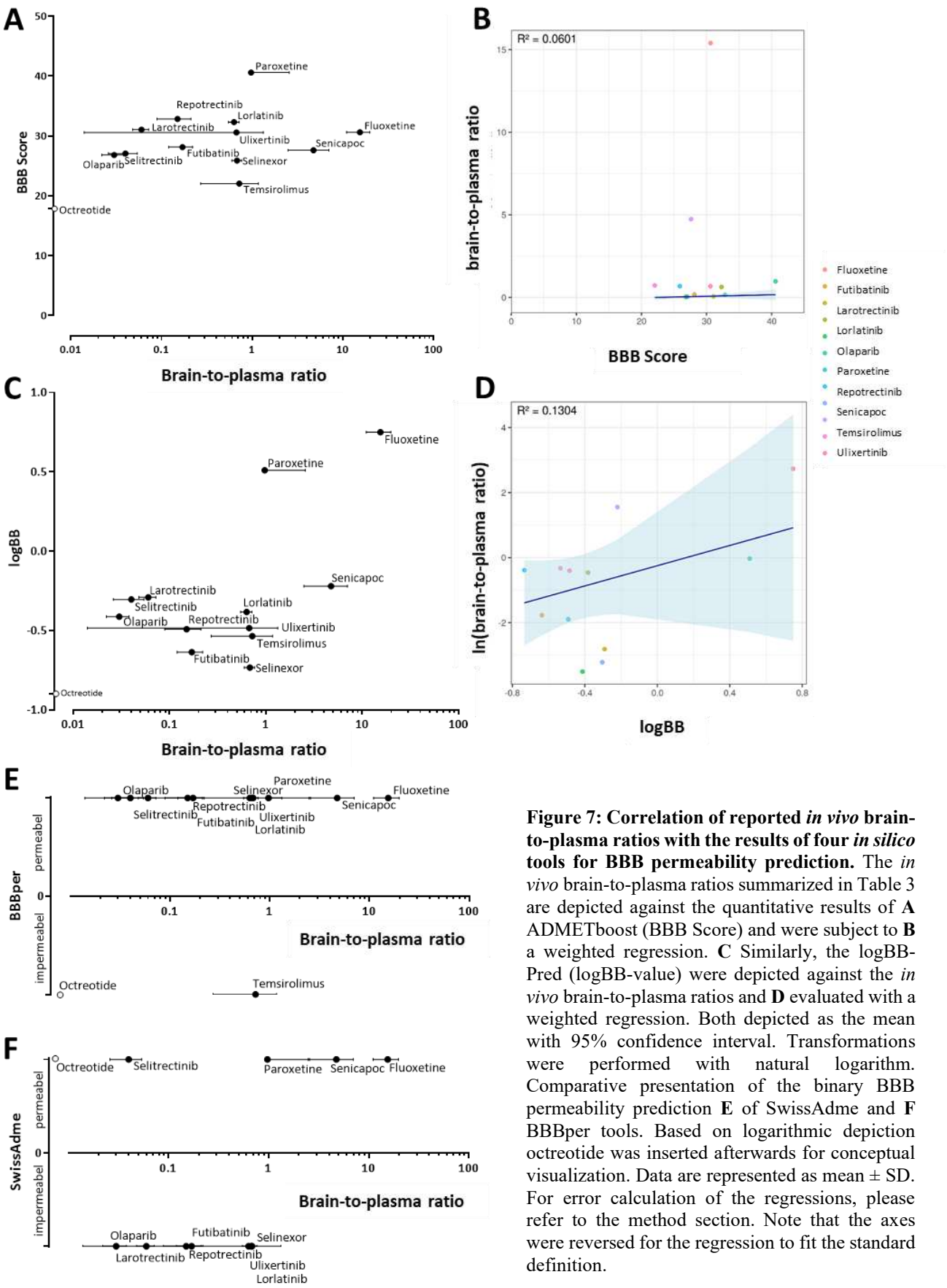

Figure 7: Correlation of reported *in vivo* brain-to-plasma ratios with the results of four *in silico* tools for BBB permeability prediction. The *in vivo* brain-to-plasma ratios summarized in Table 3 are depicted against the quantitative results of **A** ADMETboost (BBB Score) and were subject to **B** a weighted regression. **C** Similarly, the logBB-Pred (logBB-value) were depicted against the *in vivo* brain-to-plasma ratios and **D** evaluated with a weighted regression. Both depicted as the mean with 95% confidence interval. Transformations were performed with natural logarithm. Comparative presentation of the binary BBB permeability prediction **E** of SwissAdme and **F** BBBper tools. Based on logarithmic depiction octreotide was inserted afterwards for conceptual visualization. Data are represented as mean ± SD. For error calculation of the regressions, please refer to the method section. Note that the axes were reversed for the regression to fit the standard definition.

565 **Discussion**

566 Predicting human BBB permeability is crucial for assessing the suitability of drug candidates in addition
567 to identifying candidates with limited permeability for avoiding CNS side effects in malignancies not
568 associated with the CNS. Unfortunately, determining BBB permeability is challenging even in the
569 clinical settings, due to the restricted access to human CNS samples. Animal models show partly large
570 discrepancies especially for P-gp substrates[5-10]. Although *in vitro* models lack pharmacokinetic
571 recapitulation, they can be composed of human cells only. Complex models based on different cell types
572 of the neurovascular unite have been shown to be relevant in pathophysiological modeling[61,62]. In
573 general, accessibility to the basolateral compartment, and therefore to the sample behind the BBB,
574 decreases as complexity increases[62-64]. For example, in complex BBB-on-a-chip-models, the readout is
575 restricted to fluorescent substances[63] or requires the application of pressure[65]. However, accessibility for
576 quantification is a main quality criterion for pharmacological analysis. While larger constructs for
577 delivery strategies can be easily labeled, dependency on fluorescence hinders the evaluation of small
578 molecules, because fluorescent tags severely alter their physicochemical properties.

579

580 *The 3D BBB organoid model is accessible for UPLC-MS/MS analysis*

581 Previous readouts in the 3D BBB organoid model used herein were mainly based on imaging analysis
582 with fluorescence for marker substances, targeting constructs or 2D MS technique like MALDI for
583 exemplary uptake evaluation of two drugs[19,20,48,49]. However, not all molecules of interest can be
584 observed with fluorescence read-out and MALDI has currently limited resolution (30-50 µm[19,49]), is not
585 trivial, requires sample slicing and not all analytes ionize sufficiently. In contrast, 1D MS such as UPLC-
586 MS/MS, is the gold standard for clinical drug quantification.

587 To our knowledge a validated assay for the quantitative analysis with simple and higher-throughput-MS
588 has been lacking. The only previous 1D MS assay for BBB organoids was a binary evaluation as
589 verification for an *in silico* tool without relation to the respective limit of quantification or detection[66].
590 Due to the absence of quantitative drug uptake measurements in such organoids we established an easy,
591 reproducible and adaptable framework for quantifying a wide range of drugs in 3D BBB organoids. We

592 investigated and identified optimal organoid culture and handling conditions. Using commercially
593 available plates, the organoid generation is faster, the risk of contamination reduced, and the plate
594 precoating increases reproducibility. These plates allow for an easy medium change with minimal
595 organoid loss and eliminate the need for transfer steps. This ensures compatibility with automation,
596 when either a tilting platform or angled pipetting is available. The major bottleneck of this high-
597 throughput assay is the LC-MS/MS quantification method development with sufficient (very low) limits
598 of quantification. However, most small molecules (and peptide) quantifications are accessible by
599 standard sample processing techniques like protein precipitation using organic solvents and reverse-
600 phase chromatography, as was performed for most of the drugs in this study. Exceptions are the liquid-
601 liquid extraction for fluoxetine and the HILIC separation for D-Tyr(Me)Orn, also delivering sufficiently
602 low quantification limits. The developed options provide a blue print for preparing samples for a wide
603 range of analytes.
604 The investigation of two fluorescent model substances (Cy5 and hypericin) verified that these drugs are
605 not only attached to the outer cell layer, but indeed inside the organoid structure. These substances also
606 demonstrated a strong difference between lipophilic and hydrophilic distribution within the organoids.
607 Of note, the whole organoid lysis results in the quantification of drugs in the organoids, as well as
608 adsorbed to and in the BCEC. However, the same is true for tissue quantification *in vivo*. Drug-specific
609 variations can occur, especially in low-permeable substances, depending on the effects of perfusion and
610 washing, which could potentially result in *in vitro-in vivo* artifacts.

611 *The 3D BBB organoid model shows favorable architecture and viability on day 3 after generation*
612 The organoids were verified to be comparable to those in previous publication after the described culture
613 adaptions like using an orbital shaker, as well as the ready-to-use pre-coated plates. This was performed
614 with CLSM with respect to architecture and crucial BBB hallmark expression. While previous
615 investigations mainly focused on the overall architecture, we observed the specific morphology of
616 astrocytes and pericytes in detail and over time. We therefore optimized the staining protocols for in
617 detail imaging, including the selection of the most suitable dye and addition of sample clearing.
618 Due to the inverse and spherical architecture of the organoids, they cannot develop true BBB structure,
619 which requires pericytes to wind helically around the vessel[67,68] and the coverage with astrocyte end feet

620 over the other two cell types[69,70]. However, the presence of elongations of both cell types demonstrates
621 that they are viable cells with a morphology that resembles *in vivo* cells and that they both interact with
622 the BCEC. Organoid models do not exhibit the physiological architecture of the microvasculature,
623 unlike self-vascularizing models in microfluidic systems[63,65]. Nonetheless, compared to these models,
624 the organoids used here show a higher accessibility to the basolateral compartment by whole organoid
625 lysis, while more closely recapitulating free cell-type interaction than Transwell® models or microfluidic
626 systems without vascularization. A meaningful future comparison would be a direct performance
627 comparison of organoids with both kinds of microfluidic models – simple BCEC layers with other cell
628 types for example in matrix gel[71] and self-vascularized structures[65].
629 BCEC are the core of each BBB model and generally benefit from additional differentiation time in the
630 final BBB model setup[63,72]. The aim is to achieve a tight monolayer. The outer surface of the organoids
631 appeared to be smoother on day 3, possibly indicating closer cell contact. After day 4 a tendency for
632 more CD31+ cells on the cell layer was identified, possibly representing the formation of a multilayer
633 to some extent. In general, hCMEC/D3 exhibits contact inhibition in 2D monoculture[73], and previous
634 publications on organoids did not observe an increase in overall organoid size[20]. However, we observed
635 an increase in organoid circumference, which was most likely due to an increase in the number of
636 pericytes over time. Because all cell types exhibited positive Ki67 staining for proliferation[49], a complete
637 contact inhibition of the hCMEC/D3 in the organoids could not be assumed. Therefore, any sign of a
638 multilayer hCMEC/D3 was closely observed, although this was hampered by the strong CD31 signaling.
639 Additionally, viability was assessed by evaluating the amount of apoptosis. The main peak on day 2 and
640 the subsequent decrease can most likely be attributed to the stress of generating the organoids, which
641 includes detaching the adherent cells. Cas3 staining was sufficient for our general evaluation, however,
642 we want to note that Bell and coworkers have developed a precise and validated toxicity screening based
643 on hematoxylin staining for these organoids[49]. Importantly, not all standard *in vitro* assays for viability
644 or cytotoxicity assessment we tested were sensitive enough for single organoids, highlighting the need
645 for evaluation in the used *in vitro* model and inclusion of negative and positive controls.
646 Eventually, in combination with the evaluation of the architecture and the hCMEC/D3 monolayer, day
647 3 was identified as the optimal time point for analyses, because it offered the best balance between the

correct cell morphology, complete and smooth endothelial layer, constant size, apoptosis and existence of a single endothelial layer.

The performed culture adaption had no impact on the previously reported correct expression patterns of ZO-1 and P-gp, which is important due to the significant impact of TJ and efflux transporters on BBB permeability. However, the mere expression of a TJ marker is not a sufficient confirmation of functionality, because TJ require correct localization and architecture[74,75]. ZO-1 expression was also observed in the cytoplasm, as is often the case with hCMEC/D3 while pure expression at the cell corners would be more representative of physiological conditions[20,76,77]. Final conclusions about barrier properties can only be drawn from a functional evaluation.

The 3D BBB organoid model shows functional barrier properties

In previous studies, TJ modulation with VEGF or histamine in 3D BBB organoids resulted in a higher intraorganoidal signal of fluorescently tagged, high-molecular-weight molecules[20,61,78]. There was no relevant uptake of these paracellular markers in intact organoids, nor was there any size-dependency observed between 4 to 70 kDa[48]. Considering the highly restrictive nature of the BBB as well as the small size of average drugs, macromolecular substances are not suitable to evaluate subtle but relevant BBB impairment. However, for smaller markers, the literature is contradicting: the organoids were shown to be impermeable to larger molecules without modulation of the barrier, but free fluorescein isothiocyanate (FITC) was able to diffuse into the organoids, without significant difference compared to those organoids without BCEC[48]. Recent results also showed a basal uptake of Lucifer Yellow in intact organoids, which in contrast was increased upon treatment with TNF-α and INF-γ[79]. Similarly, difference in the incubation solution concentration of fluorescein was shown between different organoids with iPS-derived endothelial cells[80]. Similar to FITC and Lucifer Yellow, we observed low basal uptake of Cy5 and D-Tyr(Me)Orn. The latter is a previously developed dipeptide paracellular marker that can be measured with high sensitivity using UPLC-MS/MS and is highly discriminative for TJ status due to its small size[50]. Interestingly, we did not observe an increase in the intraorganoidal concentration of the marker substance when we modulated the cell connections by disruption of the calcium-dependent junctions with EGTA/EDTA, modulating the TJ with adenosine and VEGF, or

676 degrading proteins with trypsin. In contrast, these treatments in our assay resulted in decreased
677 intraorganoidal D-Tyr(Me)Orn. We hypothesize that the discrepancy's for small markers may be due to
678 wash-out phenomenon's: The small marker D-Tyr(Me)Orn can be washed out more efficient in the
679 compromised organoids masking or even reversing the uptake into the organoids during incubation. For
680 Cy5 – the fluorescent pendant to D-Tyr(Me)Orn– this results in an detectable increased amount of marker
681 in the washing solutions. However, small differences are hardly detectable due to the minimal amount
682 of substance in the organoids compared to that in the remaining uptake solution before washing.
683 Therefore, differences would only be visible after the remaining uptake solution is sufficiently diluted
684 by washing steps. This is in line with what we observed for the fluorescent marker Cy5 with a higher
685 amount detected in the washing solutions after VEGF treatment, that only is significant in step 3.

686 Interestingly, the hypericin washing solution exhibited the opposite effect. This may be due to a higher
687 hypericin amount in the compromised organoids that is resistant to wash-out due to the high
688 lipophilicity.

689 The larger marker substances, which only enter after cell connections are modulated, are more than 200
690 times larger, and therefore may show completely different behavior during washout. In addition, it is
691 worth mentioning that other protocols are restricted to three washing steps[20,48,61], if washing steps are
692 specified at all.

693 All of the assays developed herein allow for the simultaneous quantification of two analytes – one
694 intended for the drug and one for the paracellular marker – at the single organoid level. However, D-
695 Tyr(Me)Orn cannot be used as a threshold for organoid integrity. While D-Tyr(Me)Orn was able to
696 identify significant effects based on the organoid integrity in the mean, the high biological variance in
697 the untreated organoids hindered the discrimination power of the marker as a threshold on single
698 organoid level. The basal uptake of small hydrophilic molecules (D-Tyr(Me)Orn, FITC and Cy5) must
699 be considered, as it limits the use of small paracellular biomarkers for integrity control in such models.

700 The fact that hCMEC/D3 did not show a difference in permeability after EGTA treatment in the 2D
701 Transwell® assay[50] and after VEGF treatment (see supplemental Figure S6), but caused reduced D-
702 Tyr(Me)Orn concentration in the organoid model indicates a more highly developed BCEC phenotype
703 in the hCMEC/D3 layer in the organoid model. This is in accordance with the observable higher

704 expression of P-gp and ZO-1 in the 3D organoid model compared to 2D models[20]. The use of BCEC
705 with higher *in vitro* barrier properties, including the fast-growing field of iPS derived cells could
706 possibly further improve the integrity of 3D organoid models[80].

707 *Drug uptake in the 3D BBB organoids correlates with* in vivo *permeability values*

708 As the updated classification criteria for brain tumors place greater emphasis on molecular and genetic
709 alterations, personalized and targeted therapies are becoming the focus of clinical development[81,82]. One
710 example is the 2026 approval of the targeted therapy tovorafenib[83]. In light of the latest research findings
711 linking neuronal activity and Ca^{2+} signaling to glioblastoma growth[84,85], repurposing of drugs is another
712 up-to-date approach[86-88]. Based on these developments, we selected a set of drugs with different BBB
713 permeabilities, including P-gp and BCRP substrates, as well as different lipophilicity values and sizes
714 (see Table 4), in order to test the translational relevance of the organoid model.

715 Although quantification of drug uptake is the most meaningful pharmacological evaluation of a BBB
716 model, it has not been previously performed in 3D BBB organoids. For evaluating the translational
717 significance, we correlated the organoid uptake ratios on a single organoid level in equilibrium with the
718 *in vivo* BBB permeability values of the 12 drugs with measurable concentrations and reported brain-to-
719 plasma ratios (Table 3). We included all found mammalian brain-to-plasma ratios (exceptions listed in
720 the limitations), to generate a mean and achieve a representative *in vivo* permeability data set, resulting
721 in the high standard deviation seen for some drugs. The correlation of the organoid uptake ratios with
722 the reported *in vivo* values revealed a strong correlation in the Deming regression accounting for
723 uncertainties in both variables. This results in a qualified NAM, indicating its suitability for predictive
724 BBB permeability ranking.

725 The sub-analysis with pure primate and human data resulted in even higher regression coefficients.
726 Although a direct comparison between these regression analyses is not possible, based on the deviating
727 number of drugs with available *in vivo* data, a tendency of this fully human organoid model to better
728 correlate with human data can be observed.

729 Selecting the transformation with the natural logarithm allowed for a proportional consideration of
730 values across multiple orders of magnitude. Otherwise, high values would have a disproportionate

731 influence on the correlations (correction for scale imbalance). This transformation also corrects for a
732 higher standard deviation, which often increases with the magnitude of the measured values (correction
733 for heteroscedasticity). These corrections are clearly visible in the quantile-quantile plot (QQ) and
734 residual plots that fulfill the criteria for linearity, normal distribution, homoscedasticity and equal
735 weighting. With this regression, it becomes possible to perform predictions for drugs quantified in the
736 organoid, despite that the BBB organoid model can´t fully represent physiological states of the BBB due
737 to the lack of dynamic blood flow, as well as an inability to recapitulate the complex architecture, from
738 which the unique features of this barrier arise.

739 The drug quantifications showed a high interorganoidal variance, at least partly due to the already high
740 size variation between the organoids of approximately 10% adding to the expected biological variation
741 and organoid formation. This cannot be corrected by the standardized volume approximation, but in part
742 be counterbalanced by the possibility to perform more replicates based on the measurement on single
743 organoids. Previous publications often considered organoids as biological replicates[20,49,61]. Based on the
744 high variance observed here, multiple organoids from at least two independent preparations were
745 regarded reliable for drug quantification. Additionally, to reduce the influence of interorganoidal
746 variance, the mean of single time and concentration points in steady state was used for correlation
747 analysis.

748 Selecting physiologically relevant concentrations resulted partly in uptake amounts below the
749 quantification limit. Additionally, low concentrations within the organoid may be obscured by the
750 background (e.g., uptake with 180 ng/mL larotrectinib results in a background of ~ 70% of signal;
751 1,800 ng/mL in a background of ~ 10% of signal). Increasing the number of washing steps or the time
752 can increase the probability of washing artifacts and diffusion. Six washing steps were selected as a
753 trade-off between reducing background and washout time. All drugs except octreotide were measurable
754 above the background level, consistent with the negligible brain penetration of this octapeptide,
755 highlighting the ability of this NAM to model low/no brain permeability.

756 In contrast to the organoid *in vitro* model, the *in silico* models used herein did not show a correlation
757 with the *in vivo* data. However, at least two of the models (chemical descriptor-based) are among the
758 top-ranked current tools[89]. The quality of all trained models depends on the quality of the training

759 dataset. As discussed in the limitations, the BBB permeability data is of poor quality, resulting in lower
760 information content. Larger data sets are often binary, or use thresholds for combination with
761 quantitative data and are biased toward permeable drugs with lesser entries of non-permeable
762 substances. This strategy depends heavily on the selected threshold and naturally neglects relevant drugs
763 with low permeability and low effective concentration. This makes the training of quantitative models
764 extremely difficult[57,89]. Additionally, they often incorporate the physiochemical properties, which
765 regularly fail to truly determine the BBB permeability[2].

766 **Limitations:**

767 One limitation of our model is the variance in the regression which indicates uncertainty in these
768 predictions, reflected in the confidence intervals and based on the interorganoidal variance.
769 A general limitation in BBB research is the current data availability and variation in acquisition. Brain-
770 to-plasma ratios are not standardized and can differ in regard to:
771 1) Method of sampling. Typically, they are measured by quantifying the brain tissue concentration and
772 the total plasma concentration (B/P or as partition coefficient $K_{p,brain}$). For substances with high platelet
773 incorporation, determination in whole blood is more appropriate (see e.g., temsirolimus). Since only the
774 unbound fraction of a drug can reach the target, the unbound fraction ratio (B_u/P_u or unbound partition
775 coefficient $K_{p,uu,brain}$) was proposed as a more insightful parameter[90]. Quantifying unbound brain
776 concentration or the extracellular fraction is not trivial. It can also be determined in different ways, either
777 by technically challenging microdialysis[91,92] or by calculation with the beforehand identified tissue
778 binding percentage. Although not always identical, the concentration in the CSF is used as an
779 approximation of free brain concentration[90,91,93,94].
780 2) Time of sampling. Partition coefficients are determined either in steady state or after a single dose
781 with the AUC. Unfortunately, these ratios are not always established in a time-independent manner:
782 quantification of the B/P ratio after a single dose on a single time point depends highly on drug-specific
783 pharmacokinetics and, therefore, on the selected time point.
784 3) Specie and pathophysiology. Obviously, brain-to-plasma ratios are more comparable when evaluated
785 in healthy subjects. However, the ratios are often determined in the relevant disease model, which

786 frequently affects the BBB. Most human data are collected from patients included in clinical studies, as
787 seen here with the CSF samples for repotrectinib and lorlatinib. Therefore, and based on the smaller
788 assumed effect on CSF concentrations from a partly opened BBB, we included these data for our
789 correlation analysis. Data derived from tumor tissue was only included it if it was mixed with total brain
790 tissue or if it was shown to have no differences compared to healthy brain tissue. The exception was
791 temsirolimus, for which tumor tissue data were the only available tissue concentrations. For olaparib,
792 mice with tumors showed comparable results to healthy macaques[95]. The authors presumed this amount
793 to be negligible with no true brain penetration, consistent with quantifications in rats[96]. In contrast,
794 human tumor tissue showed a high concentration of olaparib with large variability, probably due to
795 BTB[96].
796 Ulixertinib exhibited low brain concentrations in healthy and tumor tissue of mice, resulting in a brain-
797 to-plasma concentration of 0.0176[53]. The first results of a clinical trial, presented in a poster, show higher
798 brain concentrations in tumor patients. The CSF-to-unbound plasma concentration was 1.33 with high
799 discrepancies in the tumor's bound ratios (enhancing region: 0.5; non-enhancing region: 0.2). However,
800 these results are still much larger than those observed in rodents[97]. This discrepancy may be due to
801 species differences often observed for P-gp substrates[5-10].
802 4) Inclusion of relevant metabolism. While we did not observe relevant generation of the active
803 metabolites of fluoxetine and temsirolimus in the organoid model, the amount of norfluoxetine is
804 included in the reported *in vivo* brain permeability. We therefore used these sums as approximations for
805 fluoxetine alone.
806 Ultimately, all these deviations may result in discrepancies in the reported brain-to-plasma ratios for a
807 drug. Improved *in vivo* data would benefit translational correlations for performance evaluation of BBB
808 models and training of *in silico* prediction tools.

809 **Conclusion**

810 This study established and validated the first UPLC-MS/MS assay for the reproducible quantification
811 of drugs in single 3D BBB organoids. This strategy generated the first pharmacological quantitative
812 evaluation of *in vitro*-to-*in vivo* translational relevance for drug BBB permeability in an organoid model

813 and qualified this strategy as a NAM for prediction and ranking of the BBB permeability of drugs *in*
814 *vivo*. This NAM was demonstrated to be superior over state-of-the-art *in silico* prediction models and
815 outperformed reported 2D BBB models. The reliable setup allows for future automation to implement
816 this NAM into routine screening of drug candidates for CNS malignancies or to select candidates with
817 low BBB permeability to avoid CNS side effects in toxicological characterization.
818
819 **Supplementary information:**

820 Supplement Table S1: Mass spectrometry and chromatography parameters for analyzed drugs.

821 Supplementary Figure S1: Representative CLSM images over culture time from day 2 to day 5 after
822 assembly.

823 Supplementary Figure S2: Representative CLSM images of astrocytes located outside the organoid
824 cover in some organoid preparations.

825 Supplementary Table S2: Validation results for D-Tyr(Me)Orn in organoid matrix.

826 Supplementary Figure S3: Representative light microscopy images of organoid lysis.

827 Supplementary Figure S4: Comparisons of direct and logarithm transformed correlations.

828 Supplementary Figure S5: Diagnostic plots for performed correlations with and without logarithmic
829 transformation.

830 Supplementary Table S3: Representative quality control results for UPLC-MS/MS drug assays.

831 Supplementary Table S4: Statistical analysis of drug uptake in organoids over time.

832 Supplementary Figure S6: Clearance volume of Transwell® experiments of D-Tyr(Me)Orn for
833 hCMEC/D3.

834 Extended Data 1: Reproducible code for regression.

835 Extended Data 2: Regression data.

836 **Author Contributions:** Conceptualization, CB, MS, GB, JW, JB; Formal analysis, CB; Funding
837 acquisition, CB, MS; Investigation, CB, EM, CS, MK, JC; Methodology, CB, JW, MS, JB, CS, GB;

838 Project administration, JB, JW, MS; Resources, JB, JW, PU, JCS; Supervision, CB, JW, MS, JB, GB;
839 Validation, CB, MS, JW, GB, JB, CS; Visualization, CB, CS; Writing – original draft, CB; Writing –
840 review & editing, JB, JW, MS, GB, CS, EM, PU, JCS, MK, JC.

841 **Funding:** This work was supported by the "Krebs-und Scharlachforschung Mannheim" and the
842 Deutsche Forschungsgemeinschaft (DFG, German Research Foundation) – Project ID 404521405, SFB
843 1389 – UNITE Glioblastoma, Work Package C01. GB was supported by the Physician Scientist and the
844 Olympia Morata program of the Faculty of Medicine of Heidelberg University.

845 **Availability of data and materials:** The data supporting the conclusions of this article is included
846 within the published article. The data for the regression curve is made available with this manuscript in
847 extended data file 2, together with an in-detail reproducible R Markdown file in extended data 1.

848 **Acknowledgments:** We thank Kevin Steimel for excellent technical assistance and the Heidelberg
849 Nikon Imaging Center for support with CLSM.

850 **AI Statement:** Perplexity AI was used to support literature research https://www.perplexity.ai/ (last
851 accessed 11.09.26), Gemini and DeepL Write for improving the English in some sections and Copilot
852 for streamlining of the R programming. The authors reviewed all suggestions and take full responsibility
853 for the final content.

854 **List of abbreviations:** ACN: acetonitrile; AGM™: Astrocyte Growth Medium with all supplements;
855 AJ: adherens junctions; ALK: anaplastic lymphoma kinase; AUC: area under the curve; BBB: blood
856 brain-barrier; BCEC: brain capillary endothelial cells; BCRP: breast cancer resistance protein; BSA:
857 bovine serum albumin; BTB: blood-tumor barrier; Cas3: cleaved caspase 3; clogP: calculated logP;
858 CLSM: confocal laser scanning microscopy; CNS: central nervous system; CID: collision-induced
859 dissociation; D-Tyr(Me)Orn: D-O-methyl-tyrosine and D-ornithine; DMSO: dimethyl sulfoxide;
860 EGM™: Endothelial Growth Medium 2 with all supplements; EDTA: ethylenediamine tetraacetic acid;
861 EGTA: ethylene glycol tetraacetic acid; ERK1/2: extracellular signal regulated kinase; ESI: electrospray
862 ionization; FA: formic acid; FBS: fetal bovine serum; FGFR: fibroblast growth factor receptor; HBSS:
863 Hanks Balanced Salt Solution; HCl: hydrochloric acid; HHBSS: HBSS with 0.01 M HEPES; IF:
864 immunofluorescence; IS: internal standard; $K_{CA}3.1$: calcium activated potassium channel; LDH: lactate

865 dehydrogenase; LPR-1: low density lipoprotein receptor-related protein 1; LLOQ: lower limit of
866 quantification; MAPK: mitogen-activated protein kinase; MRM: selected reaction monitoring; mTOR:
867 mechanistic target of rapamycin; MW: molecular weight; NaOH: sodium hydroxide; NTRK:
868 neurotrophic tyrosine receptor kinase; MALDI: matrix-assisted laser desorption/ionization; MRP2:
869 multidrug resistance associated protein 2; MW: molecular weight; NAM: New Approach
870 Methodologies; NFLU: norfluoxetine; PARP: poly(ADP-ribose)-polymerase; P-gp: P-glycoprotein;
871 PBS: phosphate-buffered saline; PM: Pericyte Medium; QC: quality control; QQ plot: quantile-quantile
872 plot; ROI: region of interest; ROS1: proto-oncogene 1; RPMI: Roswell Park Memorial Institute; SSRI:
873 selective serotonin reuptake inhibitor; TBME: tert-butyl methyl ether; TJ: tight junctions; UPLC-
874 MS/MS: ultra-performance liquid chromatography tandem mass spectrometry; VEGF: vascular
875 endothelial growth factor; ZO-1: Zonula occludens 1.

876 **Competing interests:** The authors declare no conflict of interest.

877 **Ethics approval and consent to participate:** Not applicable.

878 **Consent for publication:** Not applicable.

879

880 **References**

881 1 Pardridge, W. M. Blood-brain barrier delivery. *Drug Discov Today* **12**, 54-61,
882 doi:10.1016/j.drudis.2006.10.013 (2007).

883 2 Banks, W. A. Characteristics of compounds that cross the blood-brain barrier. *BMC Neurol* **9**,
884 doi:10.1186/1471-2377-9-S1-S3 (2009).

885 3 Sarkaria, J. N. et al. Is the blood-brain barrier really disrupted in all glioblastomas? A critical
886 assessment of existing clinical data. *Neuro Oncol* **20**, 184-191, doi:10.1093/neuonc/nox175
887 (2018).

888 4 Lockman, P. R. et al. Heterogeneous blood-tumor barrier permeability determines drug efficacy
889 in experimental brain metastases of breast cancer. *Clin Cancer Res* **16**, 5664-5678,
890 doi:10.1158/1078-0432.CCR-10-1564 (2010).

891 5 Syvänen, S. et al. Species differences in blood-brain barrier transport of three positron emission
892 tomography radioligands with emphasis on P-glycoprotein transport. *Drug Metab Dispos* **37**,
893 635-643, doi:10.1124/dmd.108.024745 (2009).

894 6 Kido, Y. et al. Species difference in brain penetration of P-gp and BCRP substrates among
895 monkey, dog and mouse. *Drug Metab Pharmacokinet* **42**, 100426,
896 doi:10.1016/j.dmpk.2021.100426 (2022).

7 Zhang, W. et al. Differential expression of ABC transporter genes in brain vessels vs. peripheral tissues and vessels from human, mouse and rat. *Pharmaceutics* **15**, 1563, doi:10.3390/pharmaceutics15051563 (2023).

8 Verscheijden, L. F. M., Koenderink, J. B., de Wildt, S. N. & Russel, F. G. M. Differences in P-glycoprotein activity in human and rodent blood-brain barrier assessed by mechanistic modelling. *Arch Toxicol* **95**, 3015-3029, doi:10.1007/s00204-021-03115-y (2021).

9 Song, H. W. et al. Transcriptomic comparison of human and mouse brain microvessels. *Sci Rep* **10**, 12358, doi:10.1038/s41598-020-69096-7 (2020).

10 Baltes, S. et al. Differences in the transport of the antiepileptic drugs phenytoin, levetiracetam and carbamazepine by human and mouse P-glycoprotein. *Neuropharmacology* **52**, 333-346, doi:10.1016/j.neuropharm.2006.07.038 (2007).

11 Wasielewska, J., Da Silva Chaves, J., White, A. & LE, O. Alzheimer's disease: Drug discovery. Chapter 7: Modeling the blood–brain barrier to understand drug delivery in Alzheimer's disease. (Exon Publications, 2020).

12 Uchida, Y. et al. Quantitative targeted absolute proteomics of human blood-brain barrier transporters and receptors. *J Neurochem* **117**, 333-345, doi:10.1111/j.1471-4159.2011.07208.x (2011).

13 Directive 2010/63/EU of the European Parliament and of the Council of 22 September 2010 on the protection of animals used for scientific purposes; Official Journal of the European Union.

14 EMA. Guideline on the principles of regulatory acceptance of 3Rs (replacement, reduction, refinement) testing approaches; 15.12.2016; [https://www.ema.europa.eu/en/documents/scientific-guideline/guideline-principles-regulatory-acceptance-3rs-replacement-reduction-refinement-testing-approaches_en.pdf; last accessed 06.06.2026].

15 FDA. Roadmap to Reducing Animal Testing in Preclinical Safety Studies. (2025) [https://www.fda.gov/files/newsroom/published/roadmap_to_reducing_animal_testing_in_preclinical_safety_studies.pdf; last accessed 15.10.2026].

16 Marshall, L. J., Bailey, J., Cassotta, M., Herrmann, K. & Pistollato, F. Poor translatability of biomedical research using animals - A narrative review. *Altern Lab Anim* **51**, 102-135, doi:10.1177/02611929231157756 (2023).

17 Marmol, I., Abizanda-Campo, S., Ayuso, J. M., Ochoa, I. & Olivan, S. Towards novel biomimetic in vitro models of the blood-brain barrier for drug permeability evaluation. *Bioengineering (Basel)* **10**, doi:10.3390/bioengineering10050572 (2023).

18 Badawi, A. H. et al. In vitro blood-brain barrier models for neuroinfectious diseases: A narrative review. *Curr Neuropharmacol* **22**, 1344-1373, doi:10.2174/1570159X22666231207114346 (2024).

19 Bergmann, S. et al. Blood-brain-barrier organoids for investigating the permeability of CNS therapeutics. *Nat Protoc* **13**, 2827-2843, doi:10.1038/s41596-018-0066-x (2018).

20 Cho, C. F. et al. Blood-brain-barrier spheroids as an in vitro screening platform for brain-penetrating agents. *Nat Commun* **8**, 15623, doi:10.1038/ncomms15623 (2017).

21 Daneman, R., Zhou, L., Kebede, A. A. & Barres, B. A. Pericytes are required for blood-brain barrier integrity during embryogenesis. *Nature* **468**, 562-566, doi:10.1038/nature09513 (2010).

22 Ben-Zvi, A. et al. Mfsd2a is critical for the formation and function of the blood-brain barrier. *Nature* **509**, 507-511, doi:10.1038/nature13324 (2014).

23 Armulik, A., Genove, G. & Betsholtz, C. Pericytes: developmental, physiological, and pathological perspectives, problems, and promises. *Dev Cell* **21**, 193-215, doi:10.1016/j.devcel.2011.07.001 (2011).

24 Winkler, E. A., Bell, R. D. & Zlokovic, B. V. Central nervous system pericytes in health and disease. *Nat Neurosci* **14**, 1398-1405, doi:10.1038/nn.2946 (2011).

25 Bell, R. D. et al. Pericytes control key neurovascular functions and neuronal phenotype in the adult brain and during brain aging. *Neuron* **68**, 409-427, doi:10.1016/j.neuron.2010.09.043 (2010).

26 Nikolakopoulou, A. M. et al. Pericyte loss leads to circulatory failure and pleiotrophin depletion causing neuron loss. *Nat Neurosci* **22**, 1089-1098, doi:10.1038/s41593-019-0434-z (2019).

27 Guerit, S. et al. Astrocyte-derived Wnt growth factors are required for endothelial blood-brain barrier maintenance. *Prog Neurobiol* **199**, 101937, doi:10.1016/j.pneurobio.2020.101937 (2021).

28 Alvarez JI, D.-D. A., Kebir H, Ifergan I, Fabre PJ, Terouz S, Sabbagh M, Wosik K, Bourbonnière L, Bernard M, van Horssen J, de Vries HE, Charron F, Prat A. The hedgehog pathway promotes blood-brain barrier integrity and CNS immune quiescence. *Science* **334**, 1727-1731 (2011).

29 Cibelli, A. et al. Cx43 carboxyl terminal domain determines AQP4 and Cx30 endfoot organization and blood brain barrier permeability. *Sci Rep* **11**, 24334, doi:10.1038/s41598-021-03694-x (2021).

30 Heithoff, B. P. et al. Astrocytes are necessary for blood-brain barrier maintenance in the adult mouse brain. *Glia* **69**, 436-472, doi:10.1002/glia.23908 (2021).

31 Sun, J. & He, Z. Interactions between astrocytes and cerebral endothelial cells in central nervous system diseases. *Biomed Pharmacother* **191**, 118516, doi:10.1016/j.biopha.2025.118516 (2025).

32 Abbott, N. J., Ronnback, L. & Hansson, E. Astrocyte-endothelial interactions at the blood-brain barrier. *Nat Rev Neurosci* **7**, 41-53, doi:10.1038/nrn1824 (2006).

33 Dohgu, S. et al. Brain pericytes contribute to the induction and up-regulation of blood-brain barrier functions through transforming growth factor-beta production. *Brain Res* **1038**, 208-215, doi:10.1016/j.brainres.2005.01.027 (2005).

34 Lippmann, E. S. et al. Derivation of blood-brain barrier endothelial cells from human pluripotent stem cells. *Nat Biotechnol* **30**, 783-791, doi:10.1038/nbt.2247 (2012).

35 Qian, T. et al. Directed differentiation of human pluripotent stem cells to blood-brain barrier endothelial cells. *Science Advances* **3**, e1701679 (2017).

36 Hayashi, Y. et al. Induction of various blood-brain barrier properties in non-neural endothelial cells by close apposition to co-cultured astrocytes. *Glia* **19**, 13-26, doi:10.1002/(sici)1098-1136(199701)19:1<13::Aid-glia2>3.0.Co;2-b (1997).

37 Orlidge, A. & D'amore, P. A. Inhibition of capillary endothelial cell growth by pericytes and smooth muscle cells. *J Cell Biol* **105**, 1455-1462 (1987).

38 Hayashi, K. et al. Effects of hypoxia on endothelial/pericytic co-culture model of the blood-brain barrier. *Regul Pept* **123**, 77-83, doi:10.1016/j.regpep.2004.05.023 (2004).

39 Hori, S., Ohtsuki, S., Hosoya, K., Nakashima, E. & Terasaki, T. A pericyte-derived angiopoietin-1 multimeric complex induces occludin gene expression in brain capillary endothelial cells through Tie-2 activation in vitro. *J Neurochem* **89**, 503-513, doi:10.1111/j.1471-4159.2004.02343.x (2004).

40 Janzer, R. C. & Raff, M. C. Astrocytes induce blood-brain barrier properties in endothelial cells. *Nature* **325**, 253-257 (1987).

41 Kuchler-Bopp S., Delaunoy J.-P., Artault J.-C., Zaepfel, M. & Dietrich, J.-B. Astrocytes induce several blood-brain barrier properties in non-neural endothelial cells. *Neuroreport* **10**, 1347-1353 (1999).

42 Sobue, K. et al. Induction of blood–brain barrier properties in immortalized bovine brain endothelial cells by astrocytic factors. *Neurosci. Res*. **35**, 155–164 (1999).

43 Nakagawa, S. et al. Pericytes from brain microvessels strengthen the barrier integrity in primary cultures of rat brain endothelial cells. *Cell Mol Neurobiol 27*, 687-694, doi:10.1007/s10571-007-9195-4 (2007).

44 Nakagawa, S. et al. A new blood-brain barrier model using primary rat brain endothelial cells, pericytes and astrocytes. *Neurochem. Int.* **54**, 253-263, doi:10.1016/j.neuint.2008.12.002 (2009).

45 Iwao, T. et al. Brain pericytes enhance MFSD2A expression and plasma membrane localization in brain endothelial cells through the PDGF-BB/PDGFRβ Signaling Pathway. *Int J Mol Sci* **26**, 5949, doi:10.3390/ijms26135949 (2025).

46 Fu, J. et al. Astrocyte-derived TGFβ1 facilitates blood-brain barrier function via non-canonical hedgehog signaling in brain microvascular endothelial cells. *Brain Sci* **11**, 77, doi:10.3390/brainsci11010077 (2021).

47 Igarashi, Y., Utsumi, H., Chiba, H., Yamada-Sasamori, Y., Tobioka, H., Kamimura, Y., Furuuchi, K., Kokai, Y., Nakagawa, T., Mori, M., Sawada, N. Glial cell line-derived neurotrophic factor induces barrier function of endothelial cells forming the blood-brain barrier. *Biochem Biophys Res Commun* **261**, 108–112 (1999).

48 Simonneau, C. et al. Investigating receptor-mediated antibody transcytosis using blood-brain barrier organoid arrays. *Fluids Barriers CNS* **18**, 43, doi:10.1186/s12987-021-00276-x (2021).

49 Bell, L. et al. Advanced tissue technologies of blood-brain barrier organoids as high throughput toxicity readouts in drug development. *Heliyon* **11**, e40813, doi:10.1016/j.heliyon.2024.e40813 (2025).

50 Bay, C. et al. Novel paracellular marker based on D-dipeptide structure for highly sensitive quantification with UPLC-MS/MS for in vitro and in vivo blood-brain barrier permeability analysis. *Fluids Barriers CNS 23*, doi:10.1186/s12987-026-00806-5 (2026).

51 Schindelin, J. et al. Fiji: an open-source platform for biological-image analysis. *Nat Methods* **9**, 676-682, doi:10.1038/nmeth.2019 (2012).

52 Kmiecik, S. W. et al. Validation of a UPLC-MS/MS method for quantifying intracellular olaparib levels in resistant ovarian cancer cells. *Pharmaceuticals* **18**, 1870, doi:10.3390/ph18121870 (2025).

1022 53 Sigaud, R. et al. The first-in-class ERK inhibitor ulixertinib shows promising activity in
1023 mitogen-activated protein kinase (MAPK)-driven pediatric low-grade glioma models. *Neuro*
1024 *Oncol* **25**, 566-579, doi:10.1093/neuonc/noac183 (2023).

1025 54 Bergamino M, S. M., Uhl P, Bay C, Meid AD, Stuß N, Burhenne J, Czock D, Blank A, Haefeli
1026 WE. Phase 1, first-in-human trial to evaluate the safety, tolerability, and pharmacokinetics of
1027 ascending single oral doses of octreotide/LipOra peptide in healthy volunteers. Poster P077, 11th
1028 German Pharm-Tox Summit 2026, *Naunyn-Schmiedeberg's Arch Pharmacol* **399** (Suppl 1), 39,
1029 doi.org/10.1007/s00210-026-05123-0 (2026).

1030 55 Kumar, P., Saini, V., Gupta, D., Chawla, P. A. & Kumar, A. BBBper: A machine learning-based
1031 online tool for blood-brain barrier (BBB) permeability prediction. *CNS Neurol Disord Drug*
1032 *Targets* **25**, 130-138, doi:10.2174/0118715273328174241007060331 (2026).

1033 56 Shaker, B. et al. A machine learning-based quantitative model (LogBB_Pred) to predict the
1034 blood-brain barrier permeability (logBB value) of drug compounds. *Bioinformatics* **39**, btad577,
1035 doi:10.1093/bioinformatics/btad577 (2023).

1036 57 Martins, I. F., Teixeira, A. L., Pinheiro, L. & Falcao, A. O. A Bayesian approach to in silico
1037 blood-brain barrier penetration modeling. *J Chem Inf Model* **52**, 1686-1697,
1038 doi:10.1021/ci300124c (2012).

1039 58 Tian, H., Ketkar, R. & Tao, P. ADMETboost: a web server for accurate ADMET prediction. *J*
1040 *Mol Model* **28**, 408, doi:10.1007/s00894-022-05373-8 (2022).

1041 59 Daina, A., Michielin, O. & Zoete, V. SwissADME: a free web tool to evaluate
1042 pharmacokinetics, drug-likeness and medicinal chemistry friendliness of small molecules. *Sci*
1043 *Rep* **7**, 42717, doi:10.1038/srep42717 (2017).

1044 60 Daina, A. & Zoete, V. A BOILED-Egg to predict gastrointestinal absorption and brain
1045 penetration of small molecules. *ChemMedChem* **11**, 1117-1121, doi:10.1002/cmdc.201600182
1046 (2016).

1047 61 Nzou, G. et al. Human cortex spheroid with a functional blood brain barrier for high-throughput
1048 neurotoxicity screening and disease modeling. *Sci Rep* **8**, 7413, doi:10.1038/s41598-018-25603-
1049 5 (2018).

1050 62 Dao, L. et al. Modeling blood-brain barrier formation and cerebral cavernous malformations in
1051 human PSC-derived organoids. *Cell Stem Cell* **31**, 818-833 e811,
1052 doi:10.1016/j.stem.2024.04.019 (2024).

1053 63 Campisi, M. et al. 3D self-organized microvascular model of the human blood-brain barrier with
1054 endothelial cells, pericytes and astrocytes. *Biomaterials* **180**, 117-129,
1055 doi:10.1016/j.biomaterials.2018.07.014 (2018).

1056 64 Katt, M. E. & Shusta, E. V. In vitro models of the blood-brain barrier: Building in physiological
1057 complexity. *Curr Opin Chem Eng* **30**, 42-52, doi:10.1016/j.coche.2020.07.002 (2020).

1058 65 Hajal, C. et al. Engineered human blood-brain barrier microfluidic model for vascular
1059 permeability analyses. *Nat Protoc* **17**, 95-128, doi:10.1038/s41596-021-00635-w (2022).

1060 66 Huang, E. T. C. et al. Predicting blood-brain barrier permeability of molecules with a large
1061 language model and machine learning. *Sci Rep* **14**, 15844, doi:10.1038/s41598-024-66897-y
1062 (2024).

1063 67 Alarcon-Martinez, L., Yemisci, M. & Dalkara, T. Pericyte morphology and function. *Histol*
1064 *Histopathol* **36**, 633-643, doi:10.14670/HH-18-314 (2021).

1065 68 Hartmann, D. A. et al. Pericyte structure and distribution in the cerebral cortex revealed by high-
1066 resolution imaging of transgenic mice. *Neurophotonics* **2**, 041402,
1067 doi:10.1117/1.NPh.2.4.041402 (2015).

1068 69 Muoio, V., Persson, P. B. & Sendeski, M. M. The neurovascular unit - concept review. *Acta*
1069 *Physiol* **210**, 790-798, doi:10.1111/apha.12250 (2014).

1070 70 Verkhratsky, A., Zorec, R. & Parpura, V. Stratification of astrocytes in healthy and diseased
1071 brain. *Brain Pathol* **27**, 629-644, doi:10.1111/bpa.12537 (2017).

1072 71 Wevers, N. R. et al. A perfused human blood-brain barrier on-a-chip for high-throughput
1073 assessment of barrier function and antibody transport. *Fluids Barriers CNS* **15**, 23,
1074 doi:10.1186/s12987-018-0108-3 (2018).

1075 72 Balzer, V. et al. Re-evaluation of the hCMEC/D3 based in vitro BBB model for ABC transporter
1076 studies. *Eur J Pharm Biopharm* **173**, 12-21, doi:10.1016/j.ejpb.2022.02.017 (2022).

1077 73 Weksler, B. B. et al. Blood-brain barrier-specific properties of a human adult brain endothelial
1078 cell line. *FASEB Journal* **19**, 1872-1874 (2005).

1079 74 Sasson, E. et al. Nano-scale architecture of blood-brain barrier tight-junctions. *Elife* **10**,
1080 doi:10.7554/eLife.63253 (2021).

1081 75 Tornavaca, O. et al. ZO-1 controls endothelial adherens junctions, cell-cell tension,
1082 angiogenesis, and barrier formation. *J Cell Biol* **208**, 821-838, doi:10.1083/jcb.201404140
1083 (2015).

1084 76 Biemans, E., Jakel, L., de Waal, R. M. W., Kuiperij, H. B. & Verbeek, M. M. Limitations of the
1085 hCMEC/D3 cell line as a model for Abeta clearance by the human blood-brain barrier. *J.*
1086 *Neurosci. Res.* **95**, 1513-1522, doi:10.1002/jnr.23964 (2017).

1087 77 Hinkel, S., Mattern, K., Dietzel, A., Reichl, S. & Muller-Goymann, C. C. Parametric
1088 investigation of static and dynamic cell culture conditions and their impact on hCMEC/D3
1089 barrier properties. *Int J Pharm* **566**, 434-444, doi:10.1016/j.ijpharm.2019.05.074 (2019).

1090 78 Paranjape, A. N., D'Aiuto, L., Zheng, W., Chen, X. & Villanueva, F. S. A multicellular brain
1091 spheroid model for studying the mechanisms and bioeffects of ultrasound-enhanced drug
1092 penetration beyond the blood–brain barrier. *Sci Rep* **14**, 1909, doi:10.1038/s41598-023-50203-
1093 3 (2024).

1094 79 Ebisawa, A. et al. Human blood-brain barrier spheroid models for the evaluation of drugs
1095 targeting brain vascular inflammation. *J. Pharmacol. Sci.* **162**, 40-49,
1096 doi:10.1016/j.jphs.2026.06.005 (2026).

1097 80 Mathew-Schmitt, S. et al. Generation of advanced blood-brain barrier spheroids using human-
1098 induced pluripotent stem cell-derived brain capillary endothelial-like cells. *Adv Biol* **9**,
1099 e2400442, doi:10.1002/adbi.202400442 (2025).

1100 81 Louis, D. N. et al. The 2021 WHO classification of tumors of the central nervous system: a
1101 summary. *Neuro Oncol* **23**, 1231-1251, doi:10.1093/neuonc/noab106 (2021).

1102 82 Louis, D. N. et al. cIMPACT-NOW update 6: new entity and diagnostic principle
1103 recommendations of the cIMPACT-Utrecht meeting on future CNS tumor classification and
1104 grading. *Brain Pathol* **30**, 844-856, doi:10.1111/bpa.12832 (2020).

1105 83 EMA; New medicine to treat paediatric low-grade glioma, 27.02.2026;
1106 [https://www.ema.europa.eu/en/news/new-medicine-treat-paediatric-low-grade-glioma; last
1107 06.06.2026].

84 Venkataramani, V. et al. Glioblastoma hijacks neuronal mechanisms for brain invasion. *Cell* **185**, 2899-2917 e2831, doi:10.1016/j.cell.2022.06.054 (2022).

85 Venkataramani, V. et al. Glutamatergic synaptic input to glioma cells drives brain tumour progression. *Nature* **573**, 532-538, doi:10.1038/s41586-019-1564-x (2019).

86 Eschen, J. T. et al. SENIPERA Phase 0/1 randomized window-of-opportunity clinical trial of SENIcapoc and PERAmpanel mono- and combination therapy of newly diagnosed glioblastoma: a trial protocol. *BMC Cancer* **26**, 667, doi:10.1186/s12885-026-15784-y (2026).

87 Hausmann, D. et al. Autonomous rhythmic activity in glioma networks drives brain tumour growth. *Nature* **613**, 179-186, doi:10.1038/s41586-022-05520-4 (2023).

88 Liu, K. H., Yang, S. T., Lin, Y. K., Lin, J. W., Lee, Y. H., Wang, J. Y., Hu, C. J., Lin, E. Y., Chen, S. M., Then, C. K., Shen, S. C. Fluoxetine, an antidepressant, suppresses glioblastoma by evoking AMPAR-mediated calcium-dependent apoptosis. *Oncotarget* **6**, 5088–5101 (2014).

89 Grant, N. et al. Blood brain barrier permeability prediction with artificial intelligence and machine learning: a meta-review and future directions. *Discov. Artif. Intell.* **5**, 254, doi:10.1007/s44163-025-00494-4 (2025).

90 Loryan, I. et al. Unbound brain-to-plasma partition coefficient, K(p,uu,brain)-a game changing parameter for CNS drug discovery and development. *Pharm Res* **39**, 1321-1341, doi:10.1007/s11095-022-03246-6 (2022).

91 Chowdhury, E. A. et al. Understanding the brain uptake and permeability of small molecules through the BBB: A technical overview. *J Cereb Blood Flow Metab* **41**, 1797-1820, doi:10.1177/0271678X20985946 (2021).

92 Benzel, J. et al. Investigating the central nervous system disposition of actinomycin D: implementation and evaluation of cerebral microdialysis and brain tissue measurements supported by UPLC-MS/MS quantification. *Pharmaceutics* **13**, 1498, doi:10.3390/pharmaceutics13091498 (2021).

93 Maurer, T. S., Debartolo, D. B., Tess, D. A. & Scott, D. O. Relationship between exposure and nonspecific binding of thirty-three central nervous system drugs in mice. *Drug Metab Dispos* **33**, 175-181, doi:10.1124/dmd.104.001222 (2005).

94 Westerhout, J., Ploeger, B., Smeets, J., Danhof, M. & de Lange, E. C. Physiologically based pharmacokinetic modeling to investigate regional brain distribution kinetics in rats. *AAPS J* **14**, 543-553, doi:10.1208/s12248-012-9366-1 (2012).

95 Groseclose, M. R. et al. Assessment of brain penetration and tumor accumulation of niraparib and olaparib: insights from multimodal imaging in preclinical models. *Sci Rep* **15**, 33670, doi:10.1038/s41598-025-18255-9 (2025).

96 Hanna, C. et al. Pharmacokinetics, safety, and tolerability of olaparib and temozolomide for recurrent glioblastoma: results of the phase I OPARATIC trial. *Neuro Oncol* **22**, 1840-1850, doi:10.1093/neuonc/noaa104 (2020).

97 Majd, N. et al. Window-of-Opportunity Trial of Ulixertinib for MAPK-Activated Lower Grade Gliomas in Adults. Poster CTNI-46 [https://biomed-valley.com/wp-content/uploads/2024/12/SNO2024ulixertinibposter110124.pdf; last accessed 15.10.2026], Society of Neuro-Oncology 29th annual meeting and education day, Houston, TX, *Neuro Oncol* **26**, Issue Supplement_8, doi.org/10.1093/neuonc/noae165.0413 (2024).

98 Eugene, A. R. Fluoxetine pharmacokinetics and tissue distribution quantitatively supports a therapeutic role in COVID-19 at a minimum dose of 20 mg per day. *F1000Research* **10**, 477, doi:10.12688/f1000research.53275.3 (2021).

99 Magalhaes, P., Alves, G., Fortuna, A., Llerena, A. & Falcao, A. Real-world clinical characterization of subjects with depression treated with antidepressant drugs focused on (non-)genetic factors, pharmacokinetics, and clinical outcomes: GnG-PK/PD-AD study. *Exp Clin Psychopharmacol* **28**, 202-215, doi:10.1037/pha0000294 (2020).

100 Gao, L. et al. A phase I, open-label, single-dose study to evaluate the effect of hepatic impairment on the pharmacokinetics and safety of futibatinib. *Clin Transl Sci* **16**, 1713-1724, doi:10.1111/cts.13585 (2023).

101 Hong, D. S. et al. Larotrectinib in adult patients with solid tumours: a multi-centre, open-label, phase I dose-escalation study. *Ann Oncol* **30**, 325-331, doi:10.1093/annonc/mdy539 (2019).

102 Chen, J. et al. Pharmacokinetics of lorlatinib after single and multiple dosing in patients with anaplastic lymphoma kinase (ALK)-positive non-small cell lung cancer: Results from a global phase I/II Study. *Clin Pharmacokinet* **60**, 1313-1324, doi:10.1007/s40262-021-01015-z (2021).

103 Novartis. Sandostatin® LAR® (2020); [https://www.novartis.com/sg-en/sites/novartis_sg/files/SandostatinLAR-Apr2020.SIN-App180620.pdf; last accessed 02.06.26].

104 Baum, J. et al. Olaparib in an ovarian cancer patient with end-stage renal disease and hemodialysis. *Cancer Chemother Pharmacol* **91**, 325-330, doi:10.1007/s00280-023-04514-x (2023).

105 Overbeek, J. K. et al. Pharmacokinetic boosting of olaparib: A randomised, cross-over study (PROACTIVE-study). *Eur J Cancer* **194**, 113346, doi:10.1016/j.ejca.2023.113346 (2023).

106 Metro, G. et al. Repotrectinib's clinical benefit and its brain penetration in a patient with meningeal carcinomatosis from G2032R-mutated ROS-1 positive non-small cell lung cancer. *Oncol Ther* **12**, 163-171, doi:10.1007/s40487-023-00251-6 (2024).

107 EMA. Assessment report Nexpovio (Selinexor). (2022). [https://www.ema.europa.eu/en/documents/variation-report/nexpovio-h-c-005127-ii-0001-g-epar-assessment-report_en.pdf; last accessed 02.06.2026].

108 Sparidans, R. W., Li, W., Schinkel, A. H. & Beijnen, J. H. Bioanalytical assay for the novel TRK inhibitor selitrectinib in mouse plasma and tissue homogenates using liquid chromatography-tandem mass spectrometry. *J Chromatogr B Analyt Technol Biomed Life Sci* 1122-1123, 78-82, doi:10.1016/j.jchromb.2019.05.026 (2019).

109 Ataga, K. I. et al. Improvements in haemolysis and indicators of erythrocyte survival do not correlate with acute vaso-occlusive crises in patients with sickle cell disease: a phase III randomized, placebo-controlled, double-blind study of the Gardos channel blocker senicapoc (ICA-17043). *Br J Haematol* **153**, 92-104, doi:10.1111/j.1365-2141.2010.08520.x (2011).

110 Pfizer Pharma GmbH; Fachinformation Torisel® 30 mg Konzentrat und Lösungsmittel zur Herstellung einer Infusionslösung. (2024). [https://figi.pfizer.de/sites/default/files/FI-10635.pdf; last accessed 02.06.26].

111 Mendzelevski, B. et al. Effect of ulixertinib, a novel ERK1/2 inhibitor, on the QT/QTc interval in patients with advanced solid tumor malignancies. *Cancer Chemother Pharmacol* **81**, 1129-1141, doi:10.1007/s00280-018-3564-1 (2018).

1193 112 Johnson, R. D., Lewis, R. J. & Angier, M. K. The distribution of fluoxetine in human fluids and
1194 tissues. *Journal of Analytical Toxicology* **31**, 409-414 (2007).

1195 113 Bolo N. et al. Brain pharmacokinetics and tissue distribution in vivo of fluvoxamine and
1196 fluoxetine by fluorine magnetic resonance spectroscopy. *Neuropsychopharmacology* **23**, 428-
1197 438 (2000).

1198 114 Karson C.N. et al. Human brain fluoxetine concentrations. *J Neuropsychiatry Clin Neurosci* **5**,
1199 322-329 (1993).

1200 115 Renshaw P.F., Guimaraes A.R., Fava M, Rosenbaum JF, Pearlman JD, Flood JG, Puopolo PR,
1201 Clancy K, Gonzalez RG. Accumulation of fluoxetine and norfluoxetine in human brain during
1202 therapeutic administration. *Am J Psychiatry* **149**, 1592-1594 (1992).

1203 116 Jermakowicz, A. M. et al. RAPID resistance to BET inhibitors is mediated by FGFR1 in
1204 glioblastoma. *Sci Rep* **14**, 9284, doi:10.1038/s41598-024-60031-8 (2024).

1205 117 Wang, X. et al. Advances on fluid shear stress regulating blood-brain barrier. *Microvasc Res*
1206 **128**, 103930, doi:10.1016/j.mvr.2019.103930 (2020).

1207 118 Sun, S., Pithavala, Y. K., Martini, J. F. & Chen, J. Evaluation of lorlatinib cerebrospinal fluid
1208 concentrations in relation to target concentrations for anaplastic lymphoma kinase (ALK)
1209 inhibition. *J Clin Pharmacol* **62**, 1170-1176, doi:10.1002/jcph.2056 (2022).

1210 119 Shaw, A. T. et al. Lorlatinib in non-small-cell lung cancer with ALK or ROS1 rearrangement:
1211 an international, multicentre, open-label, single-arm first-in-man phase 1 trial. *Lancet Oncol* **18**,
1212 1590-1599, doi:10.1016/S1470-2045(17)30680-0 (2017).

1213 120 Chen, W. et al. Pharmacokinetic study and tissue distribution of lorlatinib in mouse serum and
1214 tissue samples by liquid chromatography-mass spectrometry. *J Anal Methods Chem* 2019,
1215 7574369, doi:10.1155/2019/7574369 (2019).

1216 121 Chen, W. et al. A comprehensive analysis of metabolomics and transcriptomics reveals novel
1217 biomarkers and mechanistic insights on lorlatinib cosses the blood-brain barrier. *Front*
1218 *Pharmacol* **12**, 722627, doi:10.3389/fphar.2021.722627 (2021).

1219 122 Li, W. et al. P-glycoprotein (MDR1/ABCB1) restricts brain accumulation and cytochrome
1220 P450-3A (CYP3A) limits oral availability of the novel ALK/ROS1 inhibitor lorlatinib. *Int J*
1221 *Cancer* **143**, 2029-2038, doi:10.1002/ijc.31582 (2018).

1222 123 Csaba, Z. et al. A simple novel approach for detecting blood-brain barrier permeability using
1223 GPCR internalization. *Neuropathol Appl Neurobiol* **47**, 297-315, doi:10.1111/nan.12665
1224 (2021).

1225 124 Lewis, R. J., Kemp, P. M. & Johnson, R. D. Distribution of paroxetine in postmortem fluids and
1226 tissues. FAA, Office of Aerospace Medicine (2015).

1227 125 Silva, S. et al. Intranasal delivery of paroxetine: A preclinical study on pharmacokinetics,
1228 depressive-like behaviour, and neurochemical sex differences. *Biochem Pharmacol* **223**,
1229 116184, doi:10.1016/j.bcp.2024.116184 (2024).

1230 126 Silva, S. et al. Encapsulated escitalopram and paroxetine intranasal co-administration: In
1231 vitro/in vivo Evaluation. *Front Pharmacol* **12**, 751321, doi:10.3389/fphar.2021.751321 (2021).

1232 127 Li, W. et al. ABCB1 and ABCG2 restrict brain and testis accumulation and, alongside CYP3A,
1233 limit oral availability of the novel TRK inhibitor selitrectinib. *Mol Cancer Ther* **20**, 1173-1182,
1234 doi:10.1158/1535-7163.MCT-20-0705 (2021).

128 Roa, P. et al. Zurletrectinib is a next-generation TRK inhibitor with strong intracranial activity against NTRK fusion-positive tumours with on-target resistance to first-generation agents. *Br J Cancer* **131**, 601-610, doi:10.1038/s41416-024-02760-1 (2024).

129 Green, A. L. et al. Preclinical antitumor efficacy of selective exportin 1 inhibitors in glioblastoma. *Neuro Oncol* **17**, 697-707, doi:10.1093/neuonc/nou303 (2015).

130 Jin, L. W. et al. Repurposing the KCa3.1 inhibitor senicapoc for Alzheimer's disease. *Ann Clin Transl Neurol* **6**, 723-738, doi:10.1002/acn3.754 (2019).

131 Staal, R. G. W. et al. Inhibition of the potassium channel K(Ca)3.1 by senicapoc reverses tactile allodynia in rats with peripheral nerve injury. *Eur J Pharmacol* **795**, 1-7, doi:10.1016/j.ejphar.2016.11.031 (2017).

132 FDA. Center for drug evaluation and research; Clinical pharmacology review Torisel. (2006). [https://www.accessdata.fda.gov/drugsatfda_docs/nda/2007/022088s000_ClinPharmR.pdf; last accessed 07.06.2026].

133 Kuhn, J. G. et al. Pharmacokinetic and tumor distribution characteristics of temsirolimus in patients with recurrent malignant glioma. *Clin Cancer Res* **13**, 7401-7406, doi:10.1158/1078-0432.CCR-07-0781 (2007).

134 Korfel, A. et al. Phase II trial of temsirolimus for relapsed/refractory primary CNS lymphoma. *J Clin Oncol* **34**, 1757-1763, doi:10.1200/JCO.2015.64.9897 (2016).

135 Weiss, J. et al. Inhibition of P-glycoprotein by newer antidepressants. *J Pharmacol Exp Ther* **305**, 197-204, doi:10.1124/jpet.102.046532 (2003).

136 Gutmann H, M. D., Droulle A, Drewe J, Fahr A, Fricker G. P-glycoprotein- and mrp2-mediated octreotide transport in renal proximal tubule. *Br J Pharmacol*. **129**, 251-256 (2000).

137 Wen, P. Y. et al. Phase I/II study of erlotinib and temsirolimus for patients with recurrent malignant gliomas: North American Brain Tumor Consortium trial 04-02. *Neuro Oncol* **16**, 567-578, doi:10.1093/neuonc/not247 (2014).

138 Balakrishna, V. A. et al. Preclinical assessment of ulixertinib, a novel ERK1/2 inhibitor. *ADMET and DMPK* **5**, 212-223, doi:10.5599/admet.5.4.437 (2017).

139 Ji, N. et al. Ulixertinib (BVD-523) antagonizes ABCB1- and ABCG2-mediated chemotherapeutic drug resistance. *Biochem Pharmacol* **158**, 274-285, doi:10.1016/j.bcp.2018.10.028 (2018).

140 Sullivan, R. J. et al. First-in-Class ERK1/2 inhibitor ulixertinib (BVD-523) in patients with MAPK mutant advanced solid tumors: Results of a phase I dose-escalation and expansion Study. *Cancer Discov* **8**, 184-195, doi:10.1158/2159-8290.CD-17-1119 (2018).

141 Vo, K. T. et al. Phase II study of ulixertinib in children and young adults with tumors harboring activating mitogen-activated protein kinase pathway alterations: APEC1621J of the national cancer institute-children's oncology group pediatric MATCH trial. *JCO Precis Oncol* **8**, e2400103, doi:10.1200/PO.24.00103 (2024).

142 Long, A. et al. A phase I drug-drug interaction study to assess the effect of futibatinib on P-gp and BCRP substrates and of P-gp inhibition on the pharmacokinetics of futibatinib. *Clin Transl Sci* **17**, e70012, doi:10.1111/cts.70012 (2024).

143 Meric-Bernstam, F. et al. Futibatinib, an irreversible FGFR1-4 inhibitor, in patients with advanced solid tumors harboring FGF/FGFR aberrations: A phase I dose-expansion study. *Cancer Discov* **12**, 402-415, doi:10.1158/2159-8290.CD-21-0697 (2022).

1278 144 Wang, Y. et al. OATP1A/1B, CYP3A, ABCB1, and ABCG2 limit oral availability of the NTRK
1279 inhibitor larotrectinib, while ABCB1 and ABCG2 also restrict its brain accumulation. *Br J*
1280 *Pharmacol* **177**, 3060-3074, doi:10.1111/bph.15034 (2020).

1281 145 Laetsch, T. W. et al. Larotrectinib for paediatric solid tumours harbouring NTRK gene fusions:
1282 phase 1 results from a multicentre, open-label, phase 1/2 study. *Lancet Oncol* **19**, 705-714,
1283 doi:10.1016/S1470-2045(18)30119-0 (2018).

1284 146 Drilon A. et al. Efficacy and safety of larotrectinib in patients with tropomyosin receptor kinase
1285 fusion–positive lung cancers. *Precis Oncol* **6**, e2100418, doi:10.1200/PO.21 (2022).

1286 147 Solomon, B. J. et al. Lorlatinib versus crizotinib in patients with advanced ALK-positive non-
1287 small cell lung cancer: 5-Year outcomes from the phase III CROWN study. *J Clin Oncol* **42**,
1288 3400-3409, doi:10.1200/JCO.24.00581 (2024).

1289 148 Li, W., Sparidans, R. W., Lebre, M. C., Beijnen, J. H. & Schinkel, A. H. ABCB1 and ABCG2
1290 control brain accumulation and intestinal disposition of the novel ROS1/TRK/ALK inhibitor
1291 repotrectinib, while OATP1A/1B, ABCG2, and CYP3A limit its oral availability.
1292 *Pharmaceutics* **13**, 1761, doi:10.3390/pharmaceutics13111761 (2021).

1293 149 Wachter, F. et al. Molecular characterization of inflammatory tumors facilitates initiation of
1294 effective therapy. *Pediatrics* **148**, e2021050990, doi:10.1542/peds.2021-050990 (2021).

1295 150 Drilon, A. et al. Repotrectinib in ROS1 fusion-positive non-small-cell lung cancer. *N Engl J*
1296 *Med* **390**, 118-131, doi:10.1056/NEJMoa2302299 (2024).

1297

1298 **Table 1:** Used drug concentrations and the reported *in vivo* steady-state or c_{max}-concentrations

drug	Used concentration [ng/mL] [µM]	Steady-state/c_{max} concentration [ng/mL]
Fluoxetine	150 | 50 | 15 0.48 | 0.16 | 0.048	Human steady state 25.1; 215 (~50 % NFLU) [98,99]
Futibatinib	300 | 100 | 30 0.72 | 0.24 | 0.072	Human c_{max} ~ 100 [100]
Larotrectinib	1800 | 600 | 180 4.20 | 1.40 | 0.420	Human c_{max} in steady state 914 [101]
Lorlatinib	1500 | 500 | 150 3.69 | 1.23 | 0.369	Human c_{max} in steady state 576.5 [102]
Octreotide	100 | 10 | 1 0.098 | 0.0098 | 0.00098	Human steady state 1.56-2.97 [103]
Olaparib	50000 | 15000 | 5000 115 | 34.5 | 11.5	Human steady state c_{max} 6370 c_{max} 4740 [104,105]
Paroxetine	300 | 100 | 30 0.91 | 0.3 | 0.091	Human steady state 50.1 [99]
Repotrectinib	3000 | 1000 | 300 8.44 | 2.81 | 0.844	Human steady state 1317 [106]
Selinexor	300 | 100 | 30 0.677 | 0.226 | 0.0677	Human c_{max} 693 [107]
Selitrectinib	15000 | 5000 | 1500 39.47 | 13.16 | 3.947	Mice c_{max} 6623 [108]
Senicapoc	2000 | 666.67 | 200 6.19 | 2.06 | 0.619	Human steady state 137 [109]
Temsirolismus	2000 | 666.67 | 200 1.94 | 0.46 | 0.194	Human c_{max} ~2500 [110]
Ulixertinib	3000 | 1000 | 300 6.9 | 2.3 | 0.69	Human c_{max} and steady state 2031 [111]

1299 NFLU = norfluoxetine; c_{max} = maximum concentration.

1300 **Table 2:** Sample preparation for drug quantification

Drug	Calibration range [ng/mL]	System	Sample preparation
Fluoxetine	0.3 - 300	TQ-S1	Liquid-liquid extraction with 50 µL borat buffer (pH 9) and 700 µL TBME. After 10 min overhead shaking, 150 µL of supernatant was transferred and evaporated. Samples were redissolved in 200 µL H_2O/ACN (95/5, v/v) + 0.1% FA.
Octreotide	0.03 - 10	TQ-S2	Protein precipitation with 150 µl ACN + 0.1% FA, evaporated, redissolved in 100 µL H_2O + 0.1% FA.
Olaparib	0.1 - 300	TQ-XS	Protein precipitation with 150 µl ACN + 0.1% FA, evaporated, redissolved in 100 µL H_2O/ACN (95/5, v/v) + 0.1% FA.
Paroxetine	1 - 1000	TQ-S2	Protein precipitation with 150 µl ACN + 0.1% FA and 200 µL H_2O + 0.1% FA added.
Selinexor	0.1 - 3	TQ-S1	Protein precipitation with 100 µl ACN + 0.1% FA, evaporated, redissolved in 100 µL H_2O/ACN (95/5, v/v) + 0.1 % FA.
Senicapoc	1 - 3000	TQ-S1	Protein precipitation with 150 µl ACN + 0.1% FA, evaporated, redissolved in 100 µL H_2O/ACN (95/5, v/v) + 0.1 % FA.
Temsirolismus	0.1 - 1000	TQ-S1	Protein precipitation with 150 µl ACN + 0.1% FA and 200 µL H_2O + 0.1% FA added.
Ulixertinib	0.1 - 100	TQ-S2	Protein precipitation with 150 µl ACN + 0.1% FA and 200 µL H_2O + 0.1% FA added.
Multimethod for tyrosine kinase inhibitors (TKI)			
Futibatinib	0.03 - 30	TQ-S1	Protein precipitation with 100 µl ACN + 0.1% FA, evaporated and redissolved in 100 µL H_2O/ACN (95/5, v/v) + 0.1% FA.
Larotrectinib	0.01 - 10		
Lorlatinib	0.03 - 30		
Repotrectinib	0.01 - 10		
Selitrectinib	0.01 - 10		

1301

Table 3: Reported *in vivo* brain-to-plasma ratio of the evaluated drugs

drug mean ± SD	Brain-to-plasma ratio				
Fluoxetine **15.4 ± 4.39**	15 ± 3 human^{m}, B/P_{SS} 112	10 ± 6 human^{m}, B/P_{SS} 113	21.2 ± 16.2 human^{m}, B/P_{SS}^{c} 114	2.6 ± 1 human^{m}, B/P_{SS}^{c} 115	
Futibatinib **0.17 ± 0.05**	~0.17 ± 0.05 mice ^{BT}, B/P_{2h} 116				
Larotrectinib **0.06 ± 0.012**	0.036 ± 0.01 mice, B/P_{4h}	0.05 ± 0.02 mice, B/P_{1h} 117	0.09 ± 0.03 mice, B/P_{8h}		
Lorlatinib **0.63 ± 0.084**	0.734 ± 0.124 human$^{z.T.\ BM}$, CSF/$P_{uu,\ SS}$^{c} 102,118,119		0.7 ± 0.2 mice, B/P_{AUC} 120,121	0.46 ± 0.06 mice, B/P_{8h} 122	
Octreotid **0**	0 mice 123				
Olaparib **0.03 ± 0.008**	0.026 macaques, $K_{p,uu,brain}$	0.041 macaques, $K_{p,\ brain}$ 95	0.036 mice ^{BM}, $K_{p,\ brain}$	0.022 mice ^{BM}, $K_{p,uu,brain}$ 96	0 rat
Paroxetine **0.97 ± 1.59**	4.27 ± 2.64 human, B/P_{ss} 124	0.35 mice, $K_{p,\ brain}$	0.22 mice, $K_{p,uu,brain}$	0.38 mice, $K_{p,brain}$ 125	0.25 mice, $K_{p,uu,brain}$	0.354 mice, B/P_{AUC} 126
Repotrectinib **0.15 ± 0.06**	0.246 Human^{BM}, CSF/$P_{uu,\ SS}$^{c} 106	0.15 ± 0.03 mice, B/P_{4h} 127	0.103 ± 0.011 rat B/$P_{0,5h}$ ^{c} 128	0.091 ± 0.023 B/P_{2h} ^{c}	
Selinexor **0.68 ± 0.084**	0.72 rat (individuals), B/P_{2h}	0.82	0.62 macaques (individuals), B/P_{2h} 129	0.58	0.65
Selitrectinib **0.04 ± 0.014**	0.021 ± 0,004 mice, B/P_{4h} 108	0.058 ± 0.042 rat B/$P_{0,5h}$ ^{c} 128	0.041 ± 0.01 B/P_{2h} ^{c}		
Senicapoc **4.74 ± 2.26**	~5 5×FAD mice B/$P_{n.a.}$ 130	7.32 ± 4.84 B/P_{1h}	7.07 ± 3.35 rat B/P_{4h} 131	2.2 ± 0.4 B/$P_{uu,\ 1h}$	2.1 ± 0.4 rat B/$P_{uu,\ 4h}$
Temsirolimus **0.72 ± 0.45**	1.43 ± 0.90 Human^{BT}, tumor/ blood$_{SS}$ 133	0.0023 ± 0.0082 Human^{BT}, CSF/P_{uu}^{c} calculated with protein binding [132] 134			
Ulixertinib **0.67 ± 0.66**	0.0176 mice ^{PDX}, B/P_{AUC} 53	1.33 ± 0.42 Human^{BT}, CSF/$P_{uu,ss}$ 97			

^{c} = calculated from reported data; ^{m} = with metabolite; ^{BM} = with brain metastasis; ^{BT} = with brain tumor; ^{PDX} = BT40 Xenograft PDX; B/P = brain-to-plasma ratio; B/P_{uu} = unbound brain-to-plasma ratio; B/P_{AUC}= AUC-brain to AUC-plasma ~ B/P_{ss} = brain-to-plasma ratio in steady state ~ $K_{p,brain}$ = brain-to-plasma partition coefficient; B/$P_{uu,ss}$ = unbound brain-to-plasma ratio in steady state ~ $K_{p,uu,brain}$ = unbound brain-to-plasma partition coefficient; CSF/P_{uu}= CSF concentration-to-unbound plasma concentration; AUC = area under the curve.

1308 **Table 4:** Selected drugs and BBB relevant characteristics

drug	Mode of action	Efflux substrate	clogP MW	Relevance to brain tumor therapy
Fluoxetine	SSRI	P-gp[135]	4.57 309.3	Xenograft[88]
Octreotide	Somatostatin analog	P-gp and mrp2[136]	2.51 1019	Negative control
Olaparib	PARP inhibitor	P-gp[96]	1.24 434.5	NCT01390571[96]
Paroxetine	SSRI	P-gp[135]	4.23 329.4	Positive control
Selinexor	Exportin 1 inhibitor	-	2.68 443.3	NCT04421378
Senicapoc	K_{CA}3.1 blocker	-	3.53 323.3	SENIPERA, EU-CT: 2025–522605-37–00[86]
Temsirolismus	mTOR inhibitor	P-gp[110]	7.46 1030	[137] NCT05773326
Ulixertinib	ERK1/2; MAPK mutations inhibitor	likely P-gp and BCRP[138,139]	4.34 433.3	NCT01781429[140] NCT03698994[141] NCT05804227[97]
TKI				
Futibatinib	FGFR inhibitor	P-gp[142]	1.96 418.5	[143]
Larotrectinib	NTRK inhibitor	P-gp and BCRP[144]	2.00 428.4	NCT02637687[145] NCT02576431[146]
Lorlatinib	ALK inhibitor	P-gp[122]	1.87 406.4	[147] NCT06333899
Repotrectinib	ALK-, ROS1-, and NTRK inhibitor	P-gp and BCRP[148]	2.96 355.4	NCT04094610[149] NCT03093116[150]
Selitrectinib	NTRK inhibitor	P-gp and BCRP[127]	1.86 380.4	NCT03215511

1309 ALK: anaplastic lymphoma kinase; clogP: calculated logP with ChemDraw; ERK1/2: extracellular signal
1310 regulated kinase; FGFR: fibroblast growth factor receptor; K_{CA}3.1: calcium activated potassium channel; MAPK:
1311 mitogen-activated protein kinase; MW: molecular weight; mTOR: mechanistic target of rapamycin; NTRK:
1312 neurotrophic tyrosine receptor kinase; PARP: poly(ADP-ribose)-polymerase; ROS1: proto-oncogene 1; SSRI:
1313 selective serotonin reuptake inhibitor.

Supplementary Files

This is a list of supplementary files associated with this preprint. Click to download.

- Supplementaryinformationlegends.docx
- BayOrganoidSupplementspreprint.docx
- ExtendedData1Reproduciblecodeforregression.pdf
- ExtendedData2RegressionData.csv